Multiscale treatment of mechanical contact problems involving thin polymeric layers

Marcus G Schmidt,[1,2] Roger A Sauer,[1] and Ahmed E Ismail[1,2]

[1]AICES Graduate School, RWTH Aachen University, Aachen, Germany
[2]Aachener Verfahrenstechnik: Molecular Simulations and Transformations, Faculty of Mechanical Engineering, RWTH Aachen University, Aachen, Germany

E-mail: schmidt@aices.rwth-aachen.de, sauer@aices.rwth-aachen.de, aei@alum.mit.edu

The Version of Record is available online at doi:10.1088/0965-0393/22/4/045012.

Submitted on 9 November 2013, Accepted on 24 March 2014

Abstract. We propose a strategy to obtain a hyperelastic constitutive law for film-like systems from molecular dynamics (MD) simulations. The aim is to furnish a computationally efficient continuum model with this description of the material. In particular, two different methods are suggested, both of which consist of virtual experiments that are performed on the material to sample systematically the stress-strain relation. The latter is then fitted to a suitable functional form. We use a polymeric self-assembled monolayer, which spans a height of only a few nanometers, as a test case. Having determined the response function, we then apply it within a finite element simulation of a continuum mechanical nanoindentation problem. Several contact quantities such as normal reaction forces and the contact geometry are extracted from these calculations and are compared to those from an analogous, fully atomistic nanoindentation simulation. We find that the considered benchmark quantities as obtained from the continuum surrogate model reproduce well the corresponding values of the MD simulation.

1. Introduction

Nanotribology plays an increasingly important role in the current development of micro- (MEMS) and nanoelectromechanical (NEMS) systems for industrial applications [1]. This field is concerned with the study of phenomena like friction, wear and lubrication that occur on surfaces at length scales where individual atomic interactions become relevant. It also forms the basis on which insights into the mechanisms of macroscopic tribology can be gained. For example, almost a third of the fuel in passenger cars is consumed to overcome friction, even without considering braking friction [2]. There are in fact

abundant examples of energy wasted because of friction, which occurs in particular between mechanical components such as gears and bearings. Hence it greatly influences the design of devices containing moving parts, like motors and hard disks. Estimates suggest that as much as 4 per cent of the United States' gross national product is wasted because of the "ignorance of tribology" [3]. On a more abstract level, many problems in the natural sciences require a fundamental understanding of contact, the interaction of two nanoscale bodies that approach each other until they are separated only by a few Ångstroms. For instance, the forces caused by a rigid sphere approaching a wall are well-known [4], and remain valid even when the sphere has a radius of only a few nanometers, as verified by molecular dynamics (MD) simulations [5].

Recently, many studies have explored self-assembled monolayers (SAMs) [6], arrays of polymer chains arranged on a substrate to form films only a few nanometers thick. SAMs can enhance surfaces with additional features, such as providing protective or fouling-resistant coatings for manufacturing [5, 7, 8]. Of special interest are the purely mechanical characteristics of polymeric layers in the absence of chemical reactions, frequently investigated by means of experiments [3, 9–12] as well as simulations [13].

An important experimental technique to better understand the response of "clean" or functionalized substrates to mechanical contact is nanoindentation [14], in which a micro- or nano-sized tip-like object, referred to as the indenter, is gradually pushed down onto a specimen surface. We can then measure various quantities as a function of the indentation depth. The frictional behavior of the surface can be studied by scratching the indenter tip across the surface and monitoring the accompanying forces and structural changes. Nanoindentation problems are also a popular test case for molecular simulations and have been examined numerous times using atomistic techniques [15–18, among others], in spite of the significant computational resources required.

Another approach used is continuum contact mechanics [19, 20], which is typically concerned with describing macroscopic contact. Computational solutions [21–23] are usually obtained by solving a mechanical boundary value problem with an impenetrability condition. On the other hand, it is possible to incorporate interatomic pair potentials, such as the Lennard-Jones potential, directly into a continuum mechanical formulation [24, 25]. In this work, we build upon that approach by providing a systematic procedure to determine a hyperelastic constitutive law describing the mechanical behavior of a self-assembled monolayer.

For the sake of completeness we briefly mention some alternative multiscale strategies proposed to combine atomistic and continuum regimes in nanoscale contact mechanics, mainly for metallic and metalloid substrates. Many studies have been carried out employing hybrid simulations on a partitioned domain. There the upper zone of the surface, near the indenter, is handled by MD while the underlying, deeper layers are represented by finite elements. In these schemes, the material law for the finite-element part is usually either taken to be linear elastic with material constants taken from the literature or obtained from the Cauchy-Born rule, which is explained in [26]. For instance the work of Anciaux and Molinari [27] is based on the bridging-domain method of [28] and treats compression of Cu by a flat body near 0 K. It was subsequently extended to finite

temperatures [29]. The approach of Shan and Nackenhorst [30] is based on quasi-static nanoindentation steps using the quasicontinuum method (QC, [31]) for the MD-FEM coupling. In contrast, Wang et al. [32] carry out coupled nanoindentation simulations of a Ni substrate in a dynamic fashion at finite temperature. Another partitioned-domain approach is that of Luan and Robbins [33], who consider a two-dimensional surface-surface contact problem with rough features. Taking a different path, Smith et al. [34] define a continuum mechanical model of a Si substrate subject to nanoindentation, computing the local stress responses from a crystalline lattice underlying each finite element. Yet another approach is pursued by Eid et al. [35], who perform a finite element simulation of sphere-plane contact for Ru, enriched by special force-distance elements that model the asperities of a metallic surface. One of the few multiscale contact simulations involving polymeric materials is presented in Tan et al. [36] where the "pseudo-amorphous cell method" is used to simulate nanoindentation of a polymer substrate.

In this work, we propose a two-step procedure: first, a constitutive law for a thin self-assembled monolayer is obtained from MD simulations; second, the obtained law parameterizes a finite-element simulation of nanoindentation of a SAM. Constitutive modeling of polymeric and amorphous materials based on atomistic simulation has been frequently addressed in the literature. This is often based on virtual MD experiments carried out for a representative volume element (RVE) of a bulk material [37]. Other authors have developed microstructurally inspired constitutive laws [38, 39].

One should note, though, that a solid surface may have mechanical properties substantially different from those in the interior of the body. Thus, a constitutive law obtained for the bulk may not adequately describe the outermost layers. This is true for most polymers and especially SAMs, where the chain molecules at the surface may be arranged very differently than in a bulk sample. To take this into account, we develop a general procedure for relating deformed states, particularly of atomistic layers, to the resulting (virial) stresses and building a constitutive relation based on these data. The essential theory behind this procedure is presented in [40].

Our main goal is to define a purely continuum mechanical surrogate model that can accurately predict contact quantities, but at lower computational cost than fully atomistic models. We begin by specifying our key test case, nanoindentation of a SAM, in section 2. We then use two different methods in section 3 to obtain the stress-strain relationship for a thin-layered object like a SAM: once in a homogeneous fashion that assumes that the mechanical behavior does not change inside the film, and once under the assumption that these properties may vary as a function of height. The material laws determined by these methods are then used in a continuum mechanical nanoindentation problem solved using a finite element method. The setup and implementation of these simulations are summarized in section 4.

It is also possible to study the converse problem [9, 41]: given data from MD or a nanoindentation experiment, which constitutive law best reproduces these data? The work of Wang et al. [42] comes quite close to our procedure, studying a highly ordered SAM with relatively short chain lengths and obtaining good agreement between experimental, atomistic and continuum force curves. Differences with our work include

our more explicit focus on developing a methodology to determine the material behavior of film-like systems which are not extensible in one spatial direction, such that contact quantities can be reproduced in a continuum mechanical simulation. Furthermore, our formulation directly incorporates the nonbonded interactions between the indenter and the SAM mentioned above.

We are finally able to reproduce the considered atomistic contact quantities within uncertainties by means of a finite element simulation. In particular, as shown in section 5, the critical range of the transition between adhesive and repulsive regime in the normal force curve is fully captured up to fluctuations in the atomistic data.

2. Nanoindentation: atomistic and finite-element representations

2.1. An atomistic model of a thin polymeric layer

2.1.1. Self-assembled monolayers To construct an atomistic model of a SAM, we start with a single polymer chain whose potential energy is given by

$$\begin{aligned} V_{\text{chain}}(\mathbf{q}_1,\dots,\mathbf{q}_n) = \frac{1}{2}\sum_{i,j} k_q\big(q_{ij}-q_{ij}^0\big)^2 + \frac{1}{2}\sum_{i,j,k} k_\theta\big(\theta_{ijk}-\theta_{ijk}^0\big)^2 + \\ + \sum_{i,j,k,l}\sum_{m=1}^{5} A_m \cos^{m-1}(\phi_{ijkl}) + V_{\text{pair}}(\mathbf{q}_1,\dots,\mathbf{q}_n), \end{aligned} \tag{1}$$

where n is the number of atoms in the chain and $\mathbf{q}_i$, $i = 1,\dots,n$, denotes the position of atom i in either an all-atom or united-atom model. Furthermore, q_{ij}, θ_{ijk}, ϕ_{ijkl} are the distance, the angle and the torsion between two, three or four atoms, respectively, and a superscript zero denotes the appropriate equilibrium value. The coefficients k_q, k_θ and $A_1,\dots,A_5$ are material-specific. Besides the contributions from the fixed molecular structure, the potential energy may include additional short-ranged, non-bonded pair interactions, such as a Lennard-Jones potential. The functional form (1) is used by, for example, the Dreiding force field [43]. We note that this potential was only chosen because of its widespread use; our methodology is applicable to any similar potential.

Grafting a set of identical chains onto a Au substrate yields the full SAM system, consisting of both the polymer and substrate. More details of the construction process are given in section 4. The Hamiltonian describing the total energy is

$$H(\mathbf{q},\mathbf{p}) = K(\mathbf{p}) + V_{\text{int}}(\mathbf{q}) + V_{\text{ext}}(\mathbf{q}), \tag{2}$$

with the kinetic part $K(\mathbf{p}) = \frac{1}{2}\sum_i(\mathbf{p}_i\cdot\mathbf{p}_i)/m_i$ and internal energy V_{int}, which is a combination of intra-chain energies V_{chain}. The bonds, angles, and torsions between the polymer chains and the substrate atoms are subsumed in the external part V_{ext} of the potential energy. As the substrate itself is assumed to be perfectly rigid, there are no corresponding degrees of freedom included in the formalism, essentially prescribing a fixed boundary condition for the attached polymer chains. Hence V_{ext} is neither translationally nor rotationally invariant, which is the motivation for splitting the potential energy into internal and external parts. We neglect long-range interactions such as electrostatics in

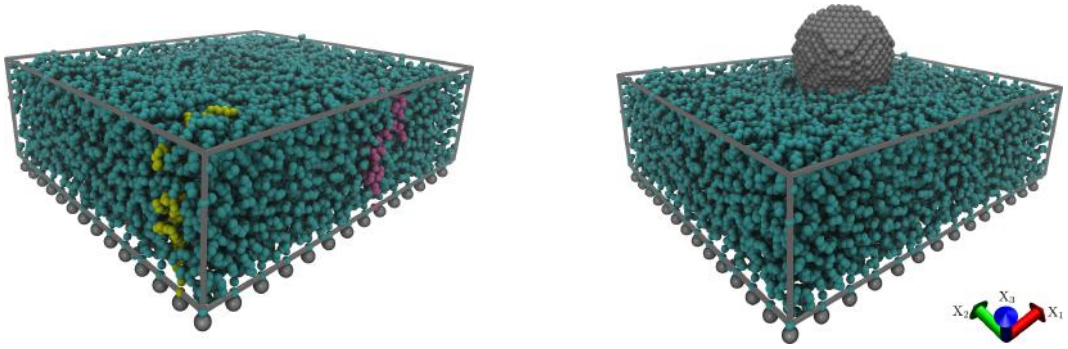

(a) (b)

Figure 1: Self-assembled monolayer which is periodic in the X_1- and X_2-directions. (a) shows the reference configuration, with two examplarily highlighted chain molecules. (b) illustrates the atomistic nanoindentation problem. Graphics have been created with [44, 45].

the total energy; this is reasonable for united-atom and coarse-grained models in which individual "atoms" are electrically neutral. This implies that the material behavior in one region is only mildly influenced by neighboring regions. A typical snapshot of an equilibrated SAM is shown in figure 1a. The total number of repeat units in the monolayer is $N = n \cdot N_c$, where N_c is the number of chains and n was the number of repeat units per chain.

2.1.2. Formulation of the atomistic nanoindentation problem To study the compatibility of appropriate atomistic and continuum formulations, we consider nanoindentation as a benchmark problem. We represent the indenter as a sphere carved from a face-centered cubic lattice interacting with the monolayer through a Lennard-Jones potential. As a simplification, the indenter is treated as a rigid body, with its atoms at fixed relative positions. Denoting the indenter atoms by $\tilde{\mathbf{q}}_1, \ldots, \tilde{\mathbf{q}}_{\widetilde{N}}$ and the LJ potential between indenter and SAM by ϕ, the total energy of the atomistic problem is obtained by augmenting the external portion V_{ext} in equation 2 by the following contact contribution:

$$V_{\text{c}}(\mathbf{q}) = \sum_{i=1}^{N} \sum_{j=1}^{\widetilde{N}} \phi(\|\mathbf{q}_i - \tilde{\mathbf{q}}_j\|), \qquad \phi(r) = 4\varepsilon \left[\left(\frac{\sigma}{r}\right)^{12} - \left(\frac{\sigma}{r}\right)^{6} \right] \quad \text{(Lennard-Jones)} \tag{3}$$

The indenter starts off far enough above the surface such that all pairwise interactions between SAM and indenter vanish. The indenter is gradually moved toward the surface (figure 1b) by controlling its position. Using MD, we can compute all quantities of interest from simulations, including forces, and in particular the force normal to the surface plane needed to push the sphere into the polymer layer, as well as geometric quantities such as the contact radius and the gap between the bodies. We restrict ourselves to quasi-static situations by allowing sufficient time to lapse between displacement steps so that thermodynamic equilibrium is attained before continuing. Numerical measurements are then carried out on equilibrated states.

2.2. An analogous continuum mechanical model problem

2.2.1. Problem definition We now briefly describe the analogous nanoindentation problem using continuum mechanics.Our formulation is based on the *body-force* approach of Sauer and Wriggers [25], which the reader should consult for further details, including some additional approaches to increase efficiency.

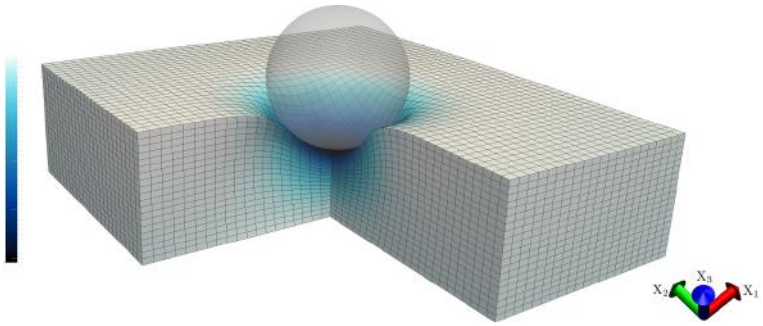

Figure 2: Finite element solution of the discretized continuum mechanical model problem. Colors indicate the displacement in X_3-direction. Image created with [46].

In its reference configuration, the SAM is a cuboid $\mathcal{B}_0^{(1)}$ oriented along Cartesian axes with the same dimensions as the atomistic model. The indenter is modeled as an undeformable sphere with domain $\mathcal{B}_0^{(2)}$. Since the indenter sphere is rigid, it can be included analytically in the expression for the system's energy, thereby requiring neither additional degrees of freedom nor meshing. Shown schematically in figure 2, the discretized continuum problem is cast as a minimization problem:

$$\begin{aligned} \Pi[\boldsymbol{\varphi}] &:= \Pi_{\text{int}}[\boldsymbol{\varphi}] + \Pi_c[\boldsymbol{\varphi}], \\ \Pi_{\text{int}}[\boldsymbol{\varphi}] &:= \int_{\mathcal{B}_0^{(1)}} \widehat{W}(\nabla\boldsymbol{\varphi}(\mathbf{X}), \mathbf{X})\, \mathrm{d}\mathbf{X} \\ \Pi_c[\boldsymbol{\varphi}] &:= \int_{\mathcal{B}_0^{(1)}} \beta_0^{(1)}(\mathbf{X}) \int_{\mathcal{B}_0^{(2)}} \beta_0^{(2)}\, \phi(\|\boldsymbol{\varphi}(\mathbf{X}) - \mathbf{Y}\|)\, \mathrm{d}\mathbf{Y}\, \mathrm{d}\mathbf{X}, \end{aligned} \tag{4}$$

where Π is the continuous energy functional and the function $\boldsymbol{\varphi} : \mathcal{B}_0^{(1)} \to \mathbb{R}^3$ is the unknown deformation we wish to find. The solution deformation $\boldsymbol{\varphi}^*$ minimizes Π over the affine space of functions satisfying the Dirichlet and periodic boundary conditions:

$$\min_{\boldsymbol{\varphi}} \Pi[\boldsymbol{\varphi}] \quad \text{subject to boundary conditions} \tag{5}$$

In this formulation, the energy functional involves an *internal* part, which requires the existence of a hyperelastic strain energy density $\widehat{W}(\mathbf{F}, \mathbf{X})$. In appendix B, we consider the circumstances under which such a hyperelastic description for a polymer is justified. Second, Π_c denotes the *contact energy* stemming from the interaction between monolayer and indenter, written as a double integral over all pairs of points in the two bodies. The quantities $\beta_0^{(1)}$ and $\beta_0^{(2)}$ give the number of particles per unit volume in the reference configurations of the monolayer and indenter, respectively.

For the SAM cuboid, the particle density $\beta_0^{(1)}$ depends on the position $\mathbf{X}$ in the reference configuration. For example, we expect the density to be small close to the free surface and increase with depth. For a spherical indenter, $\beta_0^{(2)}$ is assigned a constant value corresponding to the particle density of its crystal lattice. The pair potential ϕ appearing in Π_c is the same as in the atomistic simulation. For this case, the inner integral in Π_c can be evaluated to a closed-form expression, see [25]. This approach is only valid for pair potentials; generalizations to n-body potentials using n-fold integrals would have to be well-conceived due to integration over singularities. Strictly speaking, Π_c models a potential energy rather than a free energy, neglecting entropic effects of increasing depth.

Using this formulation, a series of quasi-static problems is solved. Displacement control is achieved by decreasing the X_3-position of the sphere $\mathcal{B}_0^{(2)}$ in each indentation step, bringing it closer to the SAM $\mathcal{B}_0^{(1)}$. The nonlinear minimization problem (5) is solved using Newton's iteration based on the derivatives of Π. The associated strong form is given by

$$\mathrm{Div}_{\mathbf{X}}\, \widehat{\mathbf{P}}(\nabla\boldsymbol{\varphi}(\mathbf{X}), \mathbf{X}) + \widehat{\mathbf{B}}[\boldsymbol{\varphi}](\mathbf{X}) = \mathbf{0}, \quad \mathbf{X} \in \mathcal{B}_0^{(1)}. \tag{6}$$

where, as the missing link between atomistic and continuum simulations, the functional expression $\widehat{\mathbf{P}}$ for the first Piola-Kirchhoff stress remains indeterminate.

2.2.2. Relationship to analytical contact models For the case of continuum mechanical sphere-plane contact, several researchers have derived analytical expressions for the resulting forces and interaction geometry, all of which involve additional assumptions and approximations and are therefore adequate only in certain situations. Szlufarska et al. [1] give a review, describing some of the most notable representatives, known as Hertz theory [47], JKR [48], DMT [49], Maugis-Dugdale [50], Persson theory [51] and TCCM [52]. They all have in common that they use as an input the (effective) Young's modulus, which limits them to isotropic linear constitutive laws and small deformations. The differences in our approach are:

(i) Our approach in principle permits arbitrary non-linear constitutive laws that can also involve spatial inhomogeneities.

(ii) The general continuum problem (5) is solved numerically instead of giving analytical formulas that rely on major additional assumptions. This allows the treatment of arbitrarily shaped domains undergoing finite deformations.

The limitations of analytical contact theories are studied in detail in Luan and Robbins [53]. Nevertheless, good agreement between MD curves and these analytical models has been reported for SAMs [13, 15] and crystalline surfaces [54, 55]. There, material properties were eliminated *a posteriori* to phenomenologically match particular quantities of a nanoindentation problem. In contrast, our aim is to develop an approach that determines a material model *in advance*, which can then be used in contact mechanical calculations without further parameter fitting.

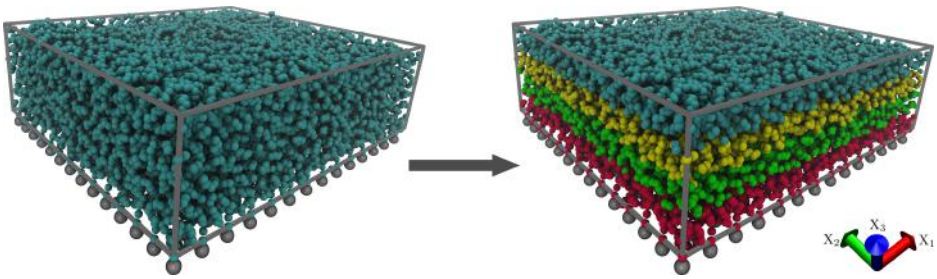

Figure 3: The self-assembled monolayers is subdivided into $L = 4$ sublayers.

3. Constitutive relations for thin layers

As mentioned in section 2.2.1, to describe the mechanical equilibrium behavior of a material we still need a hyperelastic constitutive relation for the stress $\widehat{\mathbf{P}}(\mathbf{F}, \mathbf{X})$ accompanying a local deformation $\mathbf{F}$ at point $\mathbf{X}$. We would like to obtain this information using a procedure applicable to layer-like structures like our SAM, which can have arbitrary in-plane extensions in the X_1- and X_2-directions, but has a fixed out-of-plane height in the X_3-direction. Moreover, the procedure should be general and uncoupled from any specific application problem.

We now determine the stress-strain relation for the SAM using atomistic simulations based on molecular dynamics. Traditionally, one would construct a representative volume element (RVE) and study its response to systematically applied deformations [37, 56–58]. However, this requires construction of a fully periodic three-dimensional bulk that captures the material's effective mechanical behavior. But in our case, the system lacks periodicity in one dimension as the height of a self-assembled monolayer depends entirely on the arrangement and the length of its chains, and consequently does not admit the construction of arbitrarily sized RVEs. We consider two alternatives to overcome this difficulty, both based on deformation simulations. The size of the system in this case should be representative, so that no strong finite-size effects occur, but not so large that the computational cost becomes prohibitive. The obtained material characteristics can then be used in finite element simulations of monolayers with larger extent in the X_1- and X_2-directions, so we can also think of the SAM system as a representative surface element (RSE). Related concepts have been studied, for example, in [59].

In section 3.2 we propose a method that treats the layer as being perfectly homogeneous, holding the atoms in an upper and lower region rigid to close the system with alternative, fixed boundary conditions. This can be seen as a natural adaption of the RVE concept. The method is then refined in section 3.3, where we take into account that the mechanical properties of the SAM may not be perfectly homogeneous, but can depend on height. In this context, the monolayer will be divided into several sublayers, as shown in figure 3, and individual material properties will be determined in each sublayer. In the following, we refer to these two approaches as the single-layer and multilayer method, respectively. Both methods apply *virtual deformation experiments* to the atomistic reference configuration of the SAM, causing an overall change in shape that we call a *deformed* configuration.

In both methods, we will specify the *second* Piola-Kirchhoff stress as a function of the right Cauchy-Green deformation tensor $\mathbf{C} = \mathbf{F}^T\mathbf{F}$:

$$\mathbf{S} = \widehat{\mathbf{S}}(\mathbf{C}, \mathbf{X}) = \bar{\mathbf{S}}(\mathbf{C}; \boldsymbol{\lambda}(\mathbf{X})) \tag{7}$$

This is the more convenient way to formulate constitutive laws obeying material frame-indifference. Here, $\bar{\mathbf{S}}$ denotes some particular chosen functional form for the stress that depends on material-specific parameters $\boldsymbol{\lambda} = (\lambda_1, \ldots, \lambda_q) \in \mathbb{R}^q$. In the single-layer method, we assume the material is homogeneous and thus the parameter vector $\boldsymbol{\lambda}$ is independent of $\mathbf{X}$, whereas the multilayer method divides the full layer along its height into L sublayers and assigns parameter vectors $\boldsymbol{\lambda}^{(1)}, \ldots, \boldsymbol{\lambda}^{(L)}$ to each sublayer so that $\boldsymbol{\lambda}(\mathbf{X}) = \boldsymbol{\lambda}^{(l)}$ for a material point $\mathbf{X}$ located in sublayer l. Once these parameters have been found they can be used in subsequent finite element simulations. However, we are currently concerned only with characterizing the SAM itself, and thus disregard the details of the application problems. We now must explore how mechanical quantities like stresses and deformations can be expressed in terms of the positions and momenta of individual atoms; the theory of equilibrium statistical mechanics [60, 61] is naturally employed for this purpose. Any omitted implementation details in the remainder of this section are described in section 4.

3.1. Reference configuration of atoms

We perform a molecular dynamics simulation of the SAM set up in section 2.1.1. A metallic substrate is present, but the indenter tip is not (figure 1a). The system is equilibrated in the canonical (NVT) ensemble kept at a fixed temperature of $T_0 = 300\,\mathrm{K}$. We define an *atomistic reference configuration* $\mathcal{A}_0$ as the set of the mean positions of the atoms at equilibrium, cf. [40]:

$$\mathcal{A}_0 \equiv \{\overline{\mathbf{Q}}_i\} = \{\langle \mathbf{q}_i \rangle\}, \quad i = 1, \ldots, N \tag{8}$$

As individual polymer strands are grafted onto the substrate and only limited thermal energy is available, the possible trajectories are restricted. Hence, the mean values in (8) are well-defined. The equilibrated system may be not completely stress-free, as a result of the grafting, the non-periodicity of the simulation domain in X_3-direction, and use of the canonical ensemble. More precisely, the average value of the virial stress $\boldsymbol{\sigma}$, defined in section 3.2, need not vanish identically, but will instead often have non-zero residual stress components. For example, σ_{33} can have a positive (tensile) value as the grafted polymer chains tend to explore the free space above the SAM. Also, the normal stress components in the X_1- and X_2-directions σ_{11} and σ_{22} may become non-zero as a result of fluctuating spacing between chains. These in-plane stresses can thus be controlled by modifying the spacing. However, we found in our simulations that stress components for the reference configuration are typically small compared to the stresses when the system undergoes deformations. Therefore, we neglect this residual stress and proceed as if it were exactly zero. The effect of non-negligible pre-stress in nanoindentation is further examined in Schall and Brenner [62], while the possibility of defining a fictitious

unstressed configuration is explored in [63]. If the reference configuration $\mathcal{B}_0^{(1)}$ of the continuum surrogate problem defined in 2.2.1 is to coincide with the domain $\mathcal{A}_0$ of the atomistic reference configuration, then the former will represent a natural state. Therefore the relationship $\bar{\mathbf{S}}(\mathbf{I};\boldsymbol{\lambda}) = \mathbf{0}$ yielded by typical functional forms of the stress is a good approximation of possibly pre-existing stress.

3.2. Single-layer method: Deformations of representative surface elements

Consider a SAM made up of $c_1 \times c_2$ polymer chains, where c_1 and c_2 are the number of chains in the X_1- and X_2-directions along the substrate surface. We assume that the SAM system has properties similar to those obtained from a larger sample of the same material. We now study the stress response to a prescribed deformation gradient $\mathbf{F}$, where $\mathbf{F} = \mathbf{I}$ refers to the undeformed reference configuration. In the classical case of a fully periodic, three-dimensional RVE one would deform the original simulation box $\Omega_0 = \{\sum_{i=1}^3 \omega_i \mathbf{A}_i \,|\, \omega_i \in [0,1]\}$ of the MD model by transforming it to $\Omega(\mathbf{F}) = \mathbf{F}\Omega_0 = \{\sum_{i=1}^3 \omega_i \mathbf{a}_i \,|\, \omega_i \in [0,1]\}$ with $\mathbf{a}_i = \mathbf{F}\mathbf{A}_i$, $i = 1,2,3$. $\mathbf{A}_i$ and $\mathbf{a}_i$ denote the edge vectors spanning the reference and the deformed parallelepiped, respectively. In the case of a film, periodic boundary conditions only apply to the first two dimensions and additional boundary conditions are required. One particular virtual deformation experiment consists in imposing a homogeneous deformation described by the deformation gradient $\mathbf{F}$ as follows. We choose $X_3 = 0$ to define the SAM's bottom interface with the underlying substrate. For heights a, b satisfying $0 < a < b$, let

$$\mathcal{P}_{\text{down}} := \big\{\, i \mid 0 \le \overline{Q}_{i,3} \le a \big\}, \quad \mathcal{P}_{\text{up}} := \big\{\, i \mid b \le \overline{Q}_{i,3} \big\} \tag{9}$$

denote sets of atoms in some (thin) lower and upper layer, respectively. We now drive each boundary atom $i \in \mathcal{P}_{\text{up}} \cup \mathcal{P}_{\text{down}}$ to $\bar{\mathbf{q}}_i = \mathbf{F} \cdot \overline{\mathbf{Q}}_i$ by applying the transformation to its position in the last timestep after equilibration. The transition is carried out very slowly, so that the deformation process can be treated as isothermal, as the system has enough time to reach temperature T_0 following each infinitesimal strain increment. An abrupt imposition would instead correspond to an effectively adiabatic process with large temperature fluctuations over short time spans. The simulation box is concurrently transformed to the corresponding parallelepiped. Consquently, the region occupied by the freely moving atoms $\mathcal{P}_{\text{free}} = \{1,\dots,N\} \setminus (\mathcal{P}_{\text{up}} \cup \mathcal{P}_{\text{down}})$ attains the shape prescribed by $\mathbf{F}$. These "Dirichlet" boundary conditions are schematically illustrated in figure 4. Afterwards, we allow the system to equilibrate in the new restricted configuration. To compute the stress, we invoke the following relation for hyperelastic materials:

$$\mathbf{P}(\mathbf{F},T) = \frac{1}{V_0}\frac{\partial \Psi(\mathbf{F},T)}{\partial \mathbf{F}}, \qquad \boldsymbol{\sigma}(\mathbf{F},T) = (\det \mathbf{F})^{-1}\, \mathbf{P}(\mathbf{F},T)\, \mathbf{F}^T \tag{10}$$

where Ψ denotes the Helmholtz free energy and V_0 the reference volume of the system. In equilibrium statistical mechanics, it holds that $\Psi = \Psi(\mathbf{F},T) = -k_B T \ln Z(\mathbf{F},T)$ for the deformation-dependent canonical partition function

$$Z(\mathbf{F},T) = \frac{1}{h^{3N} N_1! \dots N_s!} \int_{\Omega(\mathbf{F})} \int_{\mathbb{R}^{3N}} \exp(-\beta H(\mathbf{q},\mathbf{p}))\, \mathrm{d}\mathbf{q}\, \mathrm{d}\mathbf{p} \tag{11}$$

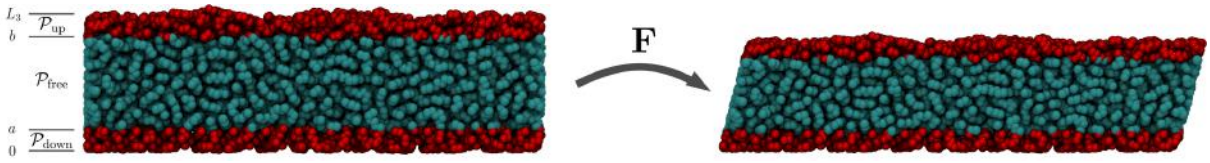

Figure 4: Homogeneous deformations $\mathbf{F}$ are prescribed on the boundary layers of the SAM. Height levels a, b separate the disjoint regions of fixed atoms $\mathcal{P}_{\text{down}}, \mathcal{P}_{\text{up}}$ from the freely moving ones $\mathcal{P}_{\text{free}}$. L_3 is the effective height.

where in this formula h is Planck's constant, H is the Hamiltonian from (2), $\beta = (k_B T)^{-1}$ and N_i is the number of atoms of type i, with $\sum_{i=1}^{s} N_i = N$. As detailed in Ray and Rahman [64] and Tadmor and Miller [40], computing the derivative of Ψ in (10) yields the virial expression for the Cauchy stress as a phase average

$$\boldsymbol{\sigma}(\mathbf{F}, T) = -\frac{1}{V}\left\langle \sum_{i=1}^{N} \mathbf{f}_i^{\text{int}} \otimes \mathbf{q}_i + \sum_{i=1}^{N} \frac{1}{m_i} \mathbf{p}_i \otimes \mathbf{p}_i \right\rangle, \tag{12}$$

with deformed volume V and internal forces $\mathbf{f}_i^{\text{int}} = -\partial_{\mathbf{q}_i} V_{\text{int}}$. This is, for example, implemented in existing MD packages such as LAMMPS [65]. In practice, we do not sum over all N atoms but only over a subset of $N' < N$ atoms that are neither held rigid nor too close to those held rigid. The aim here is to reduce the error in the computed stresses caused by the external forces introduced through the boundary conditions. The phase average is then taken over a restricted phase space with positions only in $\Omega(\mathbf{F})$ without the fixed boundary regions. For more background we again refer to [40]. The sampling can be performed using an MD simulation where these outer atoms are excluded from time integration.

We now choose a set $\mathcal{F} = \{\mathbf{F}_{(1)}, \ldots, \mathbf{F}_{(M)}\}$ of deformation gradients and for each $\mathbf{F} \in \mathcal{F}$ transfer the SAM from its atomistic reference configuration to the homogeneously deformed state prescribed by $\mathbf{F}$. In this way, we collect the associated virial stresses $\boldsymbol{\sigma}_{(m)} = \boldsymbol{\sigma}\big(\mathbf{F}_{(m)}, T_0\big)$, $m = 1, \ldots, M$, by approximating (12) as a long time average in an MD simulation. The appropriate second Piola-Kirchhoff stress is then $\mathbf{S}_{(m)} = \det \mathbf{F}_{(m)} \cdot \mathbf{F}_{(m)}^{-1} \boldsymbol{\sigma}_{(m)} \mathbf{F}_{(m)}^{-T}$, while the right Cauchy-Green deformation tensor simply becomes $\mathbf{C}_{(m)} = \mathbf{F}_{(m)}^T \mathbf{F}_{(m)}$. To fit our collected stress-strain data pairs $\big(\mathbf{C}_{(m)}, \mathbf{S}_{(m)}\big)$, $m = 1, \ldots, M$, we minimize the least-squares objective function

$$g(\boldsymbol{\lambda}) = \frac{1}{2} \sum_{m=1}^{M} \Big\| \bar{\mathbf{S}}\big(\mathbf{C}_{(m)}; \boldsymbol{\lambda}\big) - \mathbf{S}_{(m)} \Big\|^2. \tag{13}$$

There are many suitable hyperelastic functional forms $\bar{\mathbf{S}}$ that satisfy frame-indifference and can describe various material symmetries. Here we employ the well-known anisotropic Neo-Hooke model [66] with $q = 2$, as well as the anisotropic material model of Itskov and Aksel [67]. For the special case of transverse isotropy, this latter constitutive law admits an arbitrary number s of summands for representing the second Piola-Kirchhoff stress, $\bar{\mathbf{S}}(\mathbf{C}; \boldsymbol{\lambda}) = \sum_{r=1}^{s} \bar{\mathbf{S}}_r\Big(\mathbf{C}; \mu_r, w_1^{(r)}, \alpha_r, \beta_r, \gamma_r\Big)$, amounting in a total

of $q = 5s$ free parameters. While the bulk and shear moduli appearing in the Neo-Hooke model have a clear physical interpretation, this is not the case for the Itskov-Aksel material model, where the parameters are mainly introduced by its mathematical construction.

The minimization of (13) or similar objective functions to obtain a complete constitutive law is a non-trivial task. While unique solutions exist if $\bar{\mathbf{S}}$ is linear in $\boldsymbol{\lambda}$, the objective function normally has multiple local minima [68]. We try to overcome this difficulty by applying a global optimization strategy to (13) based on the Global Optimization Toolbox version 3.1.1 of Matlab [69]. Finally, we want to note that Wang et al. [42] use a strategy partially equivalent to this single-layer approach: virtual experiments are performed on a SAM by pushing a plate down on the SAM, thus producing uniaxial test deformations. The authors' FE simulations then yield very good agreement with MD and experiment for a densely grafted n-octadecyltrichlorosilane SAM. The chain molecules in our test system are longer and therefore more likely to be found in complicated coil conformations.

3.3. Multilayer method: Determining sublayer-wise material parameters

3.3.1. Algorithm outline In the single-layer method, we assumed that the mechanical behavior is the same throughout the monolayer. In place of this strong assertion, we can instead localize the stress-strain dependence. One approach would be to "cut out" smaller portions of the large SAM system, and perform deformation simulations similar to those of the single-layer method on those regions. However, it is not clear how to accomplish this cutting-out in a physically sound way: for example, the atoms found in a fixed volume element constantly change as parts of different polymer chains enter and leave. Neglecting particles outside the volume element might also lead to significantly different trajectories since the influence of the environment increases as the considered domain shrinks. Therefore, we instead propose a more indirect approach to sample local stress-strain data.

For thin layers we have already argued that it seems reasonable to assume that the response function depends only on the depth X_3, so that $\widehat{\mathbf{S}}(\mathbf{F}, \mathbf{X}) = \widehat{\mathbf{S}}(\mathbf{F}, X_3)$. The other two components X_1, X_2 correspond to the in-plane directions, along which no difference is expected. Again we assume a certain hyperelastic functional form $\bar{\mathbf{S}}(\mathbf{F}; \boldsymbol{\lambda})$ with free parameters $\boldsymbol{\lambda} = (\lambda_1, \ldots, \lambda_q)$. Taking these parameters as dependent only on the depth in the layer, $\boldsymbol{\lambda} = \boldsymbol{\lambda}(X_3)$, yields $\widehat{\mathbf{S}}(\mathbf{F}, X_3) = \bar{\mathbf{S}}(\mathbf{F}; \boldsymbol{\lambda}(X_3))$.

Next, we partition the SAM body into a set of L thinner sublayers delimited by heights $L_3 = X_3^0 > X_3^1 > \cdots > X_3^L = 0$. Here, L_3 is the X_3-coordinate of the effective top edge of the SAM, and $X_3^L = 0$ defines its bottom interface with the underlying substrate. It is not immediately clear how L_3 should be defined, especially since the top "surface" of a self-assembled monolayer is usually rippled, see figure 1a. Instead we will determine L_3 afterwards so that we obtain the best fit to continuum calculations; we therefore refer to an *effective* L_3. We can now discretize the dependence of the parameter $\boldsymbol{\lambda}$ on X_3 by defining a step function $\boldsymbol{\lambda}(X_3) := \boldsymbol{\lambda}^{(l)}$ for $X_3 \in \left[X_3^{l-1}, X_3^l\right]$, $l = 1, 2, \ldots, L$, as

shown in figure 3. Thus at all points $\mathbf{X}$ satisfying $X_3 \in \left[X_3^{l-1}, X_3^l\right]$ the material response is given by $\mathbf{S}(\mathbf{X}) = \bar{\mathbf{S}}\big(\nabla\boldsymbol{\varphi}(\mathbf{X}); \boldsymbol{\lambda}^{(l)}\big)$.

To determine the unknown parameter $\boldsymbol{\lambda}^{(l)}$ that describes one of the system's sublayers we first choose a set of P randomly distributed points $\mathbf{X}^{(l,1)}, \ldots, \mathbf{X}^{(l,P)}$ that describe *representative reference points* within the reference configuration of sublayer l. Then a set of deformed configurations $\mathcal{A}_e, e = 1, \ldots, E$, of the atomistic system is obtained as will be explained in 3.3.2 and we compute local stress tensors and local deformation gradients

$$\mathbf{S}^{(l,p,e)} = \mathbf{S}^{(e)}\big(\mathbf{X}^{(l,p)}\big), \quad \mathbf{F}^{(l,p,e)} = \mathbf{F}^{(e)}\big(\mathbf{X}^{(l,p)}\big) \tag{14}$$

at the representative points $\mathbf{X}^{(l,p)}, p = 1, \ldots, P$. How these local stress and deformation measures are defined in terms of atomistic quantities is summarized in 3.3.3. Finally, we define $\mathbf{C}^{(l,p,e)} := \big(\mathbf{F}^{(l,p,e)}\big)^T \cdot \mathbf{F}^{(l,p,e)}$. Having collected a data set of pairs $(\mathbf{S}, \mathbf{C})$, we employ a least-squares parameter fitting approach for the sublayer-specific objective function:

$$g^{(l)}(\boldsymbol{\lambda}) := \frac{1}{2} \sum_{e=1}^{E} \sum_{p=1}^{P} \left\| \bar{\mathbf{S}}\big(\mathbf{C}^{(l,p,e)}; \boldsymbol{\lambda}\big) - \mathbf{S}^{(l,p,e)} \right\|^2 \tag{15}$$

The sought parameter vector $\boldsymbol{\lambda}^{(l)}$ is then defined through

$$\boldsymbol{\lambda}^{(l)} := \underset{\boldsymbol{\lambda}}{\operatorname{argmin}}\, g^{(l)}(\boldsymbol{\lambda}). \tag{16}$$

Optionally, for each virtual experiment, one can first form averages of the $\mathbf{C}^{(l,p,e)}$ and $\mathbf{S}^{(l,p,e)}$ over all points p in order to reduce the number of summands in (15).

To summarize, we track deformation gradients for a set of deformed states in the neighborhood of certain representative reference points. The local stresses at these representative points in the deformed states are computed concurrently, as shown in figure 5. We then capture this stress-strain relationship in a constitutive equation $\mathbf{S} = \bar{\mathbf{S}}(\mathbf{C}; \boldsymbol{\lambda})$ that depends on the layer-specific parameter $\boldsymbol{\lambda}$.

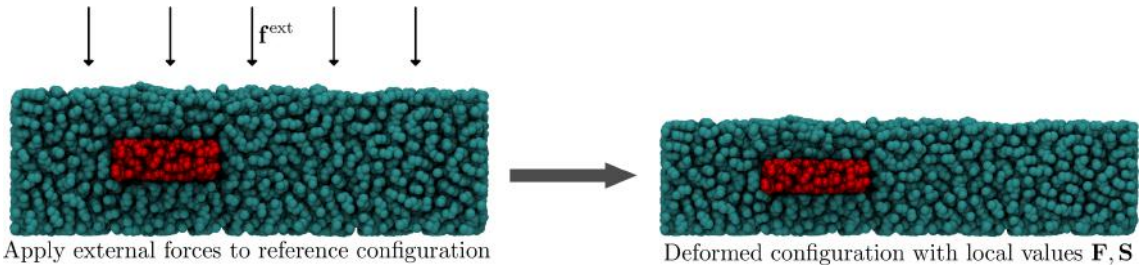

Figure 5: Localized deformation gradients and stress measures in the deformed state of a virtual deformation experiment are used to obtain a layer-wise constitutive law.

3.3.2. Virtual deformation experiments Producing deformed configurations $\mathcal{A}$ that deviate from the (nearly) stress-free atomistic reference configuration $\mathcal{A}_0$ is achieved using a series of virtual deformation experiments which can be defined arbitrarily, having only to lead to a deformed state of the system. Here, we consider virtual experiments that either

exert additional forces or prescribe Dirichlet boundary conditions on a set of boundary atoms. These choices, however, are by no means unique and other sets of experiments could also be conceived. The lone requirement is that the resulting strain field depends on $\mathbf{X}$ only through X_3, so that deformations are homogeneous within each sublayer but can vary between different sublayers. The deformations are again slowly applied to the system in its atomistic reference configuration, as we are interested in the system's isothermal response. After that, the system is allowed to equilibrate and attain the deformed configuration $\mathcal{A}$. In continuum mechanics, these virtual experiments correspond to solving a time-independent balance equation of linear momentum: $\operatorname{div} \boldsymbol{\sigma}(\mathbf{x}) + \mathbf{b}(\mathbf{x}) = \mathbf{0}$. Assigned external forces contribute to the body force $\mathbf{b}$ while prescribed positions correspond to Dirichlet boundary conditions.

The first family of virtual experiments coincides with the approach taken in the single-layer method (sec. 3.2): we fix the positions of the atoms in the upper and lower layers $\mathcal{P}_{\text{up}}$ and $\mathcal{P}_{\text{down}}$ defined in (9), so that they follow a prescribed deformation gradient $\mathbf{F}$, as shown in figure 4. In these virtual experiments, the local stresses can only be sampled in the region of the freely moving atoms, $\mathcal{P}_{\text{free}}$, but not within the rigid boundary layers, where stresses cease to be meaningful.

In the other type of virtual deformation experiments, an additional external force in the X_3-direction is exerted on atoms in $\mathcal{P}_{\text{up}}$:

$$\mathbf{f}_i^{\text{ext}} := \begin{pmatrix} 0 & 0 & -f_3 \end{pmatrix}^T, \quad i \in \mathcal{P}_{\text{up}}, \tag{17}$$

with a constant $f_3 > 0$. Instead of adding this force all at once, it is slowly increased. In addition, atoms in $\mathcal{P}_{\text{down}}$ are held rigid such that compression of the system in the X_3-direction will occur, while the periodic extension in the other two dimensions remains unchanged. Consequently, we expect a deformation gradient $\mathbf{F}$ with $F_{33} < 1$, and also a stress tensor component σ_{33} that is negative for $f_3 > 0$. In a similar fashion, we can also define

$$\mathbf{f}_i^{\text{ext}} := \begin{pmatrix} 0 & f_2 & 0 \end{pmatrix}^T, \quad i \in \mathcal{P}_{\text{up}}. \tag{18}$$

for all atoms in $\mathcal{P}_{\text{up}}$. This choice exerts a force on the top layer, causing it to shear in the X_2-direction. The result in this case is a nonzero component F_{23} of the deformation gradient. We do not modify the shape of the simulation box when applying these external forces. Repeating the virtual experiments for a set of different deformations or forces, a larger set of stress-strain pairs can be collected.

Carrying out a series of deformation experiments to collect stress-strain data in an atomistic simulation is obviously not restricted to SAMs, but can also be extended to other situations where a three-dimensional (bulk) RVE cannot be constructed. As a further remark, we should remember that perfect equilibrium usually can not be guaranteed in MD simulations. This is especially true for polymers, which may undergo long-lasting viscoelastic relaxation processes. Assuming that we come close enough to true equilibrium after time t^* (usually on the order of a few nanoseconds) is inherently an approximation. One plausibility check is to examine the component-wise stress curves: if they remain almost constant over a substantial time span, we may accept the output of

the simulation. Otherwise, alternative strategies for simulating the atomistic level may be needed.

3.3.3. Local atomistic deformation and stress measures We still need to measure localized deformations and stresses. To define the former, let $\mathcal{M}(\mathbf{X}_0)$ be the set of atom indices whose reference positions lie within a certain neighborhood of the material point $\mathbf{X}_0$:

$$\mathcal{M}(\mathbf{X}_0) = \big\{ i \mid \|\overline{\mathbf{Q}}_i - \mathbf{X}_0\|_* \leq 1 \big\} \tag{19}$$

with a suitable norm $\|\cdot\|_*$. We consider the atoms in this set a *local* thermodynamic subsystem, denoted $\mathcal{S}(\mathbf{X}_0)$. We now construct a second-order tensor that linearly approximates the deviation of the positions of the atoms in $\mathcal{S}(\mathbf{X}_0)$ from the reference configuration, which is the local deformation gradient $\mathbf{F}(\mathbf{X}_0)$.

To this end, consider a deformed state $\mathcal{A}$ of the full system. At equilibrium, the individual atoms in $\mathcal{S}(\mathbf{X}_0)$ will have attained new mean positions, $\bar{\mathbf{q}}_i = \langle \mathbf{q}_i \rangle$. In this situation, one possible approach to define $\mathbf{F}(\mathbf{X}_0)$ consists of finding the linear mapping $\boldsymbol{\varphi}_0$ that, in an unweighted (all masses are equal) least-squares sense, best describes the displacement of $\mathcal{S}(\mathbf{X}_0)$ from the reference positions $\overline{\mathbf{Q}}_i$. Hence, if we define $\boldsymbol{\varphi}(\mathbf{X}; \mathbf{F}, \mathbf{c}) := \mathbf{F}\mathbf{X} + \mathbf{c}$, the goal becomes to minimize the objective function

$$f(\mathbf{F}, \mathbf{c}) = \frac{1}{2} \sum_{i \in \mathcal{M}(\mathbf{X}_0)} \Big\| \bar{\mathbf{q}}_i - \boldsymbol{\varphi}\big(\overline{\mathbf{Q}}_i; \mathbf{F}, \mathbf{c}\big) \Big\|^2. \tag{20}$$

To find the pair $(\mathbf{F}_0, \mathbf{c}_0)$ which minimizes f we solve $\partial_{\mathbf{F}} f(\mathbf{F}, \mathbf{c}) = \mathbf{0}$ and $\partial_{\mathbf{c}} f(\mathbf{F}, \mathbf{c}) = \mathbf{0}$. It is straightforward to obtain

$$\begin{aligned}
\mathbf{F}_0 &= \left[\bar{\mathbf{q}}^{(2)} - \frac{1}{|\mathcal{M}(\mathbf{X}_0)|} \bar{\mathbf{q}}^{(1)} \otimes \overline{\mathbf{Q}}^{(1)} \right] \cdot \left[\overline{\mathbf{Q}}^{(2)} - \frac{1}{|\mathcal{M}(\mathbf{X}_0)|} \overline{\mathbf{Q}}^{(1)} \otimes \overline{\mathbf{Q}}^{(1)} \right]^{-1}, \\
\mathbf{c}_0 &= \frac{1}{|\mathcal{M}(\mathbf{X}_0)|} \big[\bar{\mathbf{q}}^{(1)} - \mathbf{F}_0 \cdot \overline{\mathbf{Q}}^{(1)} \big]
\end{aligned}$$

where we have used the abbreviations

$$\begin{aligned}
\bar{\mathbf{q}}^{(1)} &= \sum_{i \in \mathcal{M}(\mathbf{X}_0)} \bar{\mathbf{q}}_i, \qquad & \bar{\mathbf{q}}^{(2)} &= \sum_{i \in \mathcal{M}(\mathbf{X}_0)} \bar{\mathbf{q}}_i \otimes \overline{\mathbf{Q}}_i, \\
\overline{\mathbf{Q}}^{(1)} &= \sum_{i \in \mathcal{M}(\mathbf{X}_0)} \overline{\mathbf{Q}}_i, \qquad & \overline{\mathbf{Q}}^{(2)} &= \sum_{i \in \mathcal{M}(\mathbf{X}_0)} \overline{\mathbf{Q}}_i \otimes \overline{\mathbf{Q}}_i.
\end{aligned}$$

When we put $\boldsymbol{\varphi}_0(\mathbf{X}) := \boldsymbol{\varphi}(\mathbf{X}; \mathbf{F}_0, \mathbf{c}_0)$, the effective deformation gradient describing the transformation of $\mathcal{S}(\mathbf{X}_0)$ is just $\mathbf{F}(\mathbf{X}_0) = \partial_{\mathbf{X}} \boldsymbol{\varphi}_0(\mathbf{X}_0) \equiv \mathbf{F}_0$.

It is routine to extend this approach to find the best-approximating *quadratic* mapping

$$\boldsymbol{\varphi}(\mathbf{X}; \mathbf{G}, \mathbf{F}, \mathbf{c}) := \frac{1}{2} \mathbf{X} \cdot \mathbf{G}\mathbf{X} + \mathbf{F}\mathbf{X} + \mathbf{c} \tag{21}$$

between the reference and deformed configurations, with a third-order tensor $\mathbf{G}$. Again, an analytical expression for the optimum $(\mathbf{G}_0, \mathbf{F}_0, \mathbf{c}_0)$ can be readily derived such that the effective deformation gradient around point $\mathbf{X}_0$ is given by

$$\mathbf{F}(\mathbf{X}_0) = \partial_{\mathbf{X}} \boldsymbol{\varphi}(\mathbf{X}_0; \mathbf{G}_0, \mathbf{F}_0, \mathbf{c}_0) = \mathbf{G}_0 \mathbf{X}_0 + \mathbf{F}_0. \tag{22}$$

In our numerical tests, however, we observed that local deformation gradients $\mathbf{F}(\mathbf{X}_0)$ obtained using a quadratic ansatz differ very little from those based on a linear ansatz. The final effect on quantities of interest like the contact radius turns out to be negligible. Hence we prefer the computationally cheaper linear variant over the quadratic one. The latter has the advantage, though, that it admits fits to constitutive laws that take into account the second-order deformation gradient $\mathbf{G}$. Similar definitions of the microscopic deformation tensor have already been studied [70–72]. The main difference between these definitions and ours is that they determine individual deformation gradients for each atom, while we are interested in the mean deformation of an entire group of atoms.

The other quantity we will define is the stress around a spatial point $\mathbf{x}_0 := \boldsymbol{\varphi}_0(\mathbf{X}_0)$. A natural possibility is to restrict formula (12) to atom indices originally in $\mathcal{M}(\mathbf{X}_0)$:

$$\boldsymbol{\sigma}^{(e)}(\mathbf{x}_0, T) = -\frac{1}{V(\mathbf{x}_0)} \left\langle \sum_{i \in \mathcal{M}(\mathbf{X}_0)} \mathbf{f}_i^{\text{int}} \otimes \mathbf{q}_i + \sum_{i \in \mathcal{M}(\mathbf{X}_0)} \frac{1}{m_i} \mathbf{p}_i \otimes \mathbf{p}_i \right\rangle \tag{23}$$

where $V(\mathbf{x}_0)$ denotes the volume associated with the deformed subsystem $\mathcal{S}(\mathbf{X}_0)$. In the special case that only one sublayer ($L = 1$) was used together with fixed boundary conditions and if the full stress (12) was used, we would essentially recover the single-layer method. Besides (23), there exist several alternative definitions of localized atomistic stress measures [73, 74]. An excellent systematic overview is provided in Admal and Tadmor [75]. The final form of our algorithm is summarized in table 1.

4. Implementation details

This section briefly outlines the main steps and software components used to implement the two methods previously described. We also provide parameters and system properties that have remained unspecified until now.

4.1. Set-up of the atomistic system

We use the LAMMPS MD code [65] to simulate the atomistic model problem. The specific self-assembled monolayer studied consists of 196 chain molecules with $n = 150$ "monomers" each and is based on the force field from [76], where we signficantly increased the bond stiffness of the polymer so that the SAM develops a relatively even surface that is convenient to work with. Therefore, we model a polyethylene-like test case, rather than an actual polymer. The specific values are listed in table 2 in appendix A. In applications, the force-field parameters and the molecular structure have to be adapted to match the desired material, but the methodology remains unchanged.

A single layer of Au atoms arranged in a (111) plane of a fcc lattice acts as a substrate. Individual chains are bonded to these Au atoms as illustrated in figure 6. A total of 14×14 polymer chains form the SAM, with periodic boundary conditions applied along the X_1- and X_2-directions. In the initial configuration, all chains are fully elongated and tilt away from the metallic substrate by a fixed angle of 30°. The system is equilibrated for 3.5 ns in an NVT ensemble at a temperature of $T_0 = 300\,\text{K}$, using a damping parameter of

Obtain reference configuration: Equilibrate system without deformation boundary conditions to obtain the (undeformed) atomistic reference configuration $\mathcal{A}_0$.

Perform virtual experiments: Perform a series of virtual deformation experiments that yield different deformed configurations $\mathcal{A}_e$, $e = 1, \dots, E$.

Partition the surface into sublayers: Loop over all sublayers $l = 1, \dots, L$.

Examine representative reference points: Loop over all $\mathbf{X}^{(l,p)}$, $p = 1, \dots, P$, that are chosen from the sublayer l.

1. Around $\mathbf{X}^{(l,p)}$, consider the neighborhood $\mathcal{M}\big(\mathbf{X}^{(l,p)}\big)$ containing several atoms at $\overline{\mathbf{Q}}_i \in \mathcal{A}_0$ in the **undeformed configuration**.
2. For all atoms in $\mathcal{M}\big(\mathbf{X}^{(l,p)}\big)$, determine their mean **deformed positions** $\bar{\mathbf{q}}_i^{(e)} \in \mathcal{A}_e$ that they attain during the e^{th} virtual experiment.
3. Find the best-fitting linear or quadratic mapping $\boldsymbol{\varphi}_0^{(e)} : \mathbf{X} \mapsto \mathbf{x}$ that describes the transformation of the mean positions $\overline{\mathbf{Q}}_i$ to $\bar{\mathbf{q}}_i^{(e)}$, $i \in \mathcal{M}\big(\mathbf{X}^{(l,p)}\big)$.
4. Put $\mathbf{F}^{(l,p,e)} := \partial_{\mathbf{X}} \boldsymbol{\varphi}_0^{(e)}\big(\mathbf{X}^{(l,p)}\big)$ as well as $\mathbf{C}^{(l,p,e)} := \big(\mathbf{F}^{(l,p,e)}\big)^T \cdot \mathbf{F}^{(l,p,e)}$.
5. Compute the localized Cauchy stress $\boldsymbol{\sigma}^{(l,p,e)} = \boldsymbol{\sigma}^{(e)}\big(\mathbf{x}^{(l,p,e)}, T_0\big)$ at $\mathbf{x}^{(l,p,e)} = \boldsymbol{\varphi}_0^{(e)}(\mathbf{X}^{(l,p)})$ in the deformed configuration.
6. Compute the localized second Piola-Kirchhoff stress through the relationship $\mathbf{S}^{(l,p,e)} = \det \mathbf{F}^{(l,p,e)} \cdot \big(\mathbf{F}^{(l,p,e)}\big)^{-1} \cdot \boldsymbol{\sigma}^{(l,p,e)} \cdot \big(\mathbf{F}^{(l,p,e)}\big)^{-T}$.

Within sublayer l, **fit** the obtained stress-strain samples $\big(\mathbf{S}^{(l,p,e)}, \mathbf{C}^{(l,p,e)}\big)$, $p = 1, \dots, P$, $e = 1, \dots, E$, to a functional form $\overline{\mathbf{S}}\big(\mathbf{C}; \boldsymbol{\lambda}^{(l)}\big)$ to obtain the **layer-specific parameter** $\boldsymbol{\lambda}^{(l)}$.

Table 1: Summary of multilayer method to determine a layer-wise constitutive law using atomistic inputs

100 timesteps and velocity Verlet integration with timestep $\Delta t = 1\,\text{fs}$. This equilibration stage ensures that the chains attain realistic coiled and intertwined conformations. The resulting state is then considered as the atomistic reference configuration $\mathcal{A}_0$ seen in figure 1. The system has an effective height $L_3 \approx 41\,\text{Å}$ above the Au substrate as well as extents of $L_1 \approx 121.2\,\text{Å}$ and $L_2 \approx 139.9\,\text{Å}$ in the X_1- and X_2-directions.

From here, we distinguish between two cases. Based on the equilibrated system, we can carry out the virtual experiments of either the single-layer or multilayer method to determine the material behavior of the SAM. Alternatively, we can add an indenter to our system and perform an actual nanoindentation simulation, consisting of a sequence of increasing indentation depths, yielding numerical values for the contact quantities defined in section 5. The results obtained via MD will serve as the reference values that we try to reproduce with a finite element model using our material model.

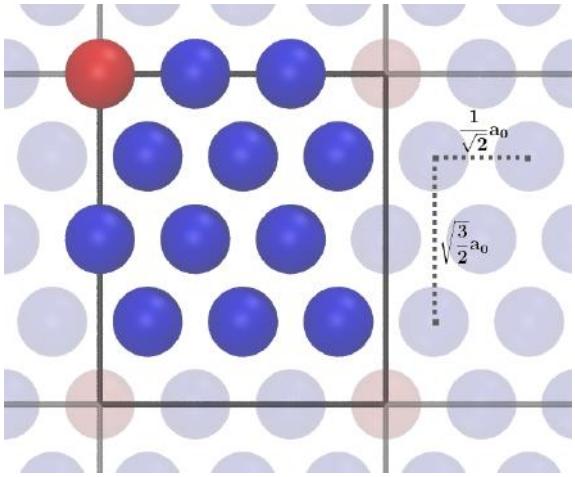

Figure 6: Schematic of the fcc (111) surface of an Au substrate (lattice constant $a_0 = 4.08\,\text{Å}$). Grid lines mark the repeating pattern in which each of the red atoms is bonded to a chain molecule.

4.2. Determination of material parameters

In the single-layer method, Dirichlet boundary conditions are applied by constraining the motion of atoms with $X_3 > 35\,\text{Å}$, which gives a restricted region $\mathcal{P}_{\text{up}}$ with a height of about 6 Å. $\mathcal{P}_{\text{down}}$ is chosen to have the same height. Then the system is deformed using the linear mapping $\mathbf{q} \mapsto \mathbf{F}_{(m)} \cdot \mathbf{Q}$, which is slowly applied to all atoms over 1 ns, with the boundary atoms in $\mathcal{P}_{\text{up}} \cup \mathcal{P}_{\text{down}}$ held fixed while the remaining atoms, which are now collectively deflected by $\mathbf{F}_{(m)} \in \mathcal{F}$, continue to move. The deformation step is followed by an additional equilibration stage of 4 ns. Afterwards, stresses, as in section 3.2, are sampled and averaged over 2 ns. In our example, the set $\mathcal{F}$ is made up of $M = 18$ different choices, covering a range of normal components $0.9 \leq F_{11}, F_{22}, F_{33} \leq 1.1$ and off-diagonal components $0 \leq F_{12}, F_{13}, F_{23} \leq 0.06$. When these simulations are completed, the objective function (13) is minimized to carry out the parameter fitting.

To identify material parameters using the multilayer method, we start from the same configuration $\mathcal{A}_0$ constructed above, and choose only force-type virtual deformation experiments, as we can actually sample stresses within the top zone of atoms, which would otherwise be at constrained positions. If we want to solve a nanoindentation problem, the mechanical characteristics of this uppermost region will be important. In particular, we apply additional normal forces in the X_3 direction in the range of 0.5 to 6.0 $\text{kcal mol}^{-1}\,\text{Å}^{-1}$ to atoms in $\mathcal{P}_{\text{up}}$, where $1\,\text{kcal mol}^{-1}\,\text{Å}^{-1} = 0.0695\,\text{nN}$. Virtual experiments involving shear have been performed with shear forces between 0.1 and 1.0 $\text{kcal mol}^{-1}\,\text{Å}^{-1}$. In our MD simulation, these forces are increased linearly from zero to their final value over a time span of 3 ns. Afterwards, the system is equilibrated for 3 ns after which it attains a deformed configuration $\mathcal{A}$ as it is restricted on all sides and thus cannot deform indefinitely. Localized stress and strain data are then collected and averaged over 2 ns. The relevant objective function for the parameter fitting is given by (15). Several algorithmic parameters can be adjusted for the multilayer method: selecting $P = 200$

random representative reference points $\mathbf{X}^{(l,p)}$ in $L = 6$ sublayers of the SAM turns out to yield reproducible fitting results. The norm that defines the neighborhood $\mathcal{M}(\mathbf{X})$ of a material point $\mathbf{X}$ in section 3.3.3 is $\|\mathbf{X}\|_* := \max\big(|X_1|/15\text{Å}, |X_2|/15\text{Å}, |X_3|/5\text{Å}\big)$. In this way a 15 Å × 15 Å × 5 Å cuboid neighborhood around $\mathbf{X}$ is assumed to exhibit continuum-like behavior. ‡

We can reproduce contact mechanical quantities to acceptable agreement using only the relatively simple Neo-Hookean material model, and employing $E = 2$ virtual deformation experiments per sublayer, one deformation resulting from applying a normal force and one from applying a shear force, as described in section 3.3.2. Note that the Neo-Hooke model has only two free parameters, the bulk modulus κ and the shear modulus μ. As it turns out, the set of virtual deformation experiments chosen—for example, the particular magnitude of applied forces—influences the identified material parameters and thus the agreement of contact quantities reproduced in the surrogate model as well. However, they all lead to qualitative agreement between the MD and FEM models. In section 5, we present the results for one of the best identified parameter sets. Both the single-layer and multilayer methods are affected by this limitation.

4.2.1. Atomistic nanoindentation simulations A sphere of radius 20 Å is added to the initial system; its rigidity corresponds to negligible indenter compliance relative to that of the SAM. The sphere is lowered normal to the monolayer in 40 steps, each of which lowers the sphere by 0.4 Å in 0.2 ns, followed by an additional 0.2 ns of relaxation time and 0.2 ns of sampling.§ This results in a total simulated time of 24 ns, where we expect to be close to thermodynamic equilibrium after each displacement, thus satisfying the quasi-static assumption.

4.2.2. Continuum mechanical nanoindentation simulations The framework (4) requires additional information when changing to a surrogate model. The monolayer geometry is represented by a cuboid $\mathcal{B}_0^{(1)}$ with the same extent $L_1 \times L_2 \times L_3$ and periodic boundary conditions as the atomistic system. However, no further geometrical features of the polymeric layer are resolved. A mesh of $50 \times 40 \times 20$ linear Lagrange elements is then used to discretize this cuboid. (Additional details on the discretization of (5) can be found in [25].) The particle density $\beta_0^{(1)}$ of the SAM is piecewise constant in X_3 with values obtained via inspection of the equilibrated atomistic system. Quadrature of high order is used such that the Lennard-Jones interactions, which exhibit a singularity as $r \to 0$, are accurately integrated. Our finite element code is based on the open source framework libMesh [77], which in turn relies on the PETSc library [78, 79]. Lastly, a series of 45 time-independent problems is solved, where in each step the center of the indenter $\mathcal{B}_0^{(2)}$ is lowered by 0.5 Å. For large indentation depths, large deformations of the reference geometry become apparent. In this regime, we sporadically observed

‡ As the virtual experiments are constructed such that the stress is expected to be a function only of X_3, we can implement the localized stresses $\boldsymbol{\sigma}^{(e)}(\mathbf{x})$ by including all atoms with the same X_3-coordinates as those in the virial expression (23), simplifying a MD implementation.

§ This corresponds to an indentation speed of 0.067 m/s, considerably faster than real experiments.

convergence problems of Newton's iteration when applied to (5). This affected the Itskov model as well as additional test runs employing a Mooney-Rivlin model, for some choices of the material parameters for both the single-layer and multilayer methods. The further investigation of this phenomenon was outside the scope of this work.

4.2.3. Validation To examine the plausibility of the material model parameters estimated by the single-layer and multilayer methods, we briefly examine a crystalline lattice of Cu atoms using the EAM force field of Foiles et al. [80]. This interatomic potential is fitted to a constant bulk modulus of $\kappa_0 = 138\,\mathrm{GPa}$. In reality, though, the bulk modulus depends on the strain. Hence, if we carry out virtual deformation experiments that induce finite strains, only the bulk modulus of that regime is calculated. We set up a block consisting of $30 \times 30 \times 30$ fcc cells of Cu with a free surface at the top. This object should be large enough so that it behaves like bulk Cu at lower heights. At $T = 50\,\mathrm{K}$, we obtain from the single-layer method a Neo-Hooke bulk modulus of $\kappa = 145\,\mathrm{GPa}$ using $M = 10$ deformation gradients, with normal and shear deformations of at most 2%. The multilayer method yields $\kappa = 143\,\mathrm{GPa}$ with fixed boundary conditions for interior sublayers and using $E = 3$ virtual experiments with deformations of 2%. When using force boundary conditions, we find $\kappa = 147\,\mathrm{GPa}$ in the interior. As noted before, the material properties calculated by either method actually depend on the deformation regime. However, for specific applications, since we may not known in advance which range of strains is most relevant, selecting the most useful virtual experiments can be difficult. Mild fluctuations exist in the bulk moduli of individual sublayers, as a result of the statistical character of the multilayer method, where data is collected at representative reference points.

5. Numerical results and discussion

The purpose of our previous considerations was to apply the constructed constitutive law to a problem involving mechanical contact. In this section, we compare MD and finite-element estimates for certain contact quantities which we define below. The resultant curves for the atomistic simulations are averaged over nine independent simulations, with different indenter positions. The estimated standard deviations are shown as error bars. All subsequent results are obtained for the fitted parameters of the constitutive laws as summarized in table 3 for the single-layer method and in table 4 for the multilayer method, both of which can be found in appendix A. In the latter we observe the expected trend of bulk and shear moduli decreasing as we move toward the free surface. This tendency, that the SAM is more compliant at the top than at the bottom, is not captured by the homogeneous single-layer concept. The parameters are not strictly monotonic, a result which may be due to the approach's statistical elements, to actual structural effects or to the time limitations for collecting response data. Also the fixed atoms at the bottom may affect the parameters identified for the lowest sublayer, but as the indentation process takes place mainly in the upper region, this is not expected to have much influence on the FEM nanoindentation simulations. Lastly, we remember that our test system is only

an example; experiments on certain types of actual SAMs suggest Young's moduli on the order of 1 GPa [11].

5.1. Normal forces

We define the total reaction force that the indenter experiences from the SAM in terms of both the atomistic results and the solution deformation $\boldsymbol{\varphi}^*$ of the FEM problem. In the first case, we obtain from equation (3) the force $\mathbf{f}_i^{\mathrm{ind}}$ exerted on monolayer atom i by the indenter. Summing these forces gives

$$\begin{aligned}\mathbf{f}_{\mathrm{at}}(t) = \sum_{i=1}^{N} \mathbf{f}_i^{\mathrm{ind}}(t) = -\sum_{i=1}^{N} \frac{\partial V_{\mathrm{c}}(\mathbf{q}(t))}{\partial \mathbf{q}_i} = \\ = -\sum_{i=1}^{N}\sum_{j=1}^{\widetilde{N}} \phi'(\|\mathbf{q}_i(t) - \widetilde{\mathbf{q}}_j(t)\|)\, \frac{\mathbf{q}_i(t) - \widetilde{\mathbf{q}}_j(t)}{\|\mathbf{q}_i(t) - \widetilde{\mathbf{q}}_j(t)\|}.\end{aligned} \tag{24}$$

This expression is then time-averaged at equilibrium: $\mathbf{f}_{\mathrm{at}} := \langle \mathbf{f}_{\mathrm{at}}(t) \rangle$. On the other hand, from the force exerted by the indenter on a continuum particle at point $\mathbf{X} \in \mathcal{B}_0^{(1)}$,

$$\widehat{\mathbf{B}}[\boldsymbol{\varphi}](\mathbf{X}) := -\int_{\mathcal{B}_0^{(2)}} \beta_0^{(2)}\, \phi'(\|\boldsymbol{\varphi}(\mathbf{X}) - \mathbf{Y}\|) \frac{\boldsymbol{\varphi}(\mathbf{X}) - \mathbf{Y}}{\|\boldsymbol{\varphi}(\mathbf{X}) - \mathbf{Y}\|} \mathrm{d}\mathbf{Y}, \tag{25}$$

we obtain the total force on the indenter:

$$\begin{aligned}\mathbf{f}_{\mathrm{cont}} = \int_{\mathcal{B}_0^{(1)}} \beta_0^{(1)}(\mathbf{X})\, \widehat{\mathbf{B}}[\boldsymbol{\varphi}^*](\mathbf{X})\, \mathrm{d}\mathbf{X} = \\ = -\int_{\mathcal{B}_0^{(1)}} \beta_0^{(1)}(\mathbf{X}) \int_{\mathcal{B}_0^{(2)}} \beta_0^{(2)}\, \phi'(\|\boldsymbol{\varphi}^*(\mathbf{X}) - \mathbf{Y}\|)\, \frac{\boldsymbol{\varphi}^*(\mathbf{X}) - \mathbf{Y}}{\|\boldsymbol{\varphi}^*(\mathbf{X}) - \mathbf{Y}\|}\, \mathrm{d}\mathbf{Y}\, \mathrm{d}\mathbf{X},\end{aligned} \tag{26}$$

which has a structure analogous to the atomistic version. Since we are dealing with sequences of quasi-static problems and, other than position control, no further forces are applied to the indenter, there is no stiction or friction present, and thus only the force component along $\mathbf{N} = (0, 0, 1)^T$ normal to the surface should be nonzero. We denote the negative of this component as $f_{\mathrm{at}}^N = -\mathbf{f}_{\mathrm{at}} \cdot \mathbf{N}$ and $f_{\mathrm{cont}}^N = -\mathbf{f}_{\mathrm{cont}} \cdot \mathbf{N}$, respectively. In figure 7a these normal forces are shown for the homogeneous approach of the single-layer method, where different fitted functional forms have been used. The forces obtained from molecular dynamics are also displayed. Using the finer resolved multilayer method, material parameters for the Neo-Hooke model have been identified for individual sublayers and the obtained normal forces are compared to MD data in figure 7b.

As the indenter approaches the surface, the force f^N between the two bodies is initially attractive, but becomes repulsive when the indenter penetrates into the monolayer. Optimal alignment of the MD and FE curves implies that the effective height of the SAM is slightly different in the two methods. Figure 7b shows that the multilayer method produces a material law consisting of Neo-Hookean sublayers leading to a convincing reproduction of the MD curves in a continuum model. The normal forces in the surrogate model remain within the standard deviation of the MD data for both the attractive and repulsive zones. Such agreement is not possible with the homogeneous

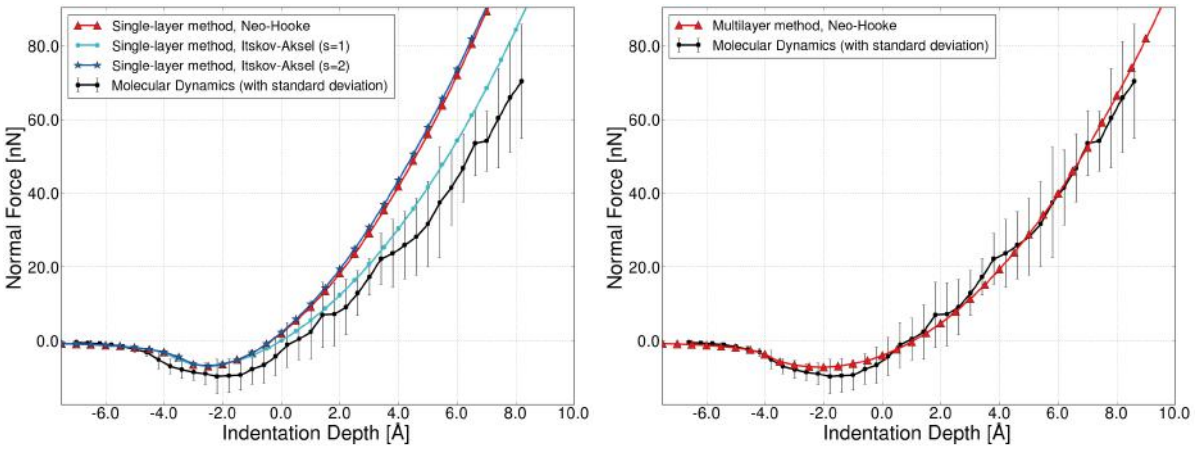

(a) (b)

Figure 7: Normal forces for (a) various material models fitted with the single-layer method and (b) a Neo-Hooke model fitted with the multilayer method. The indentation depth is negative if the sphere's lowest point is above the SAM's initial effective top edge and positive if below. Negative forces f^N are attractive; positive ones are repulsive.

single-layer method, where the continuum curves always exceed the error bars of the MD values for individual points. In particular, the transversely isotropic Itskov-Aksel model with $s = 2$ (with ten free parameters) cannot appropriately reproduce the atomistic curve, indicating that the assumption of homogeneous material behavior is too strong. As mentioned before, the curve shown for the multilayer method is based on the set of virtual deformation experiments that overall yielded the best reproduction of the MD curves presented here.

5.2. Contact radius

A geometric quantity often examined in nanoindentation is the contact radius, which measures the area of interaction between indenter and surface. We first determine the set of monolayer atoms for which the force exerted by the indenter points away from its center. These points are projected onto the X_1X_2-plane; we then define the contact radius as the radius of the smallest circle containing 90% of these points. This number is subsequently averaged over 100 snapshots per indentation level, which are taken in intervals of 2000 time steps. This definition is of course not unique; several alternatives have been suggested [13]. Our choice allows a simple finite-element analogue. We determine the set of quadrature points for which the force (25) exerted by the indenter points away from its center. We again calculate the X_1X_2-projection for these points and determine the radius of the smallest circle containing 90% of those quadrature points. In figures 8a,b the resulting contact radii for fitted homogeneous material models are compared to that of the MD simulation. The results for a continuum model consisting of fitted Neo-Hookean sublayers are shown in figures 8c,d, where again a qualitative improvement is observed from the former to the latter.

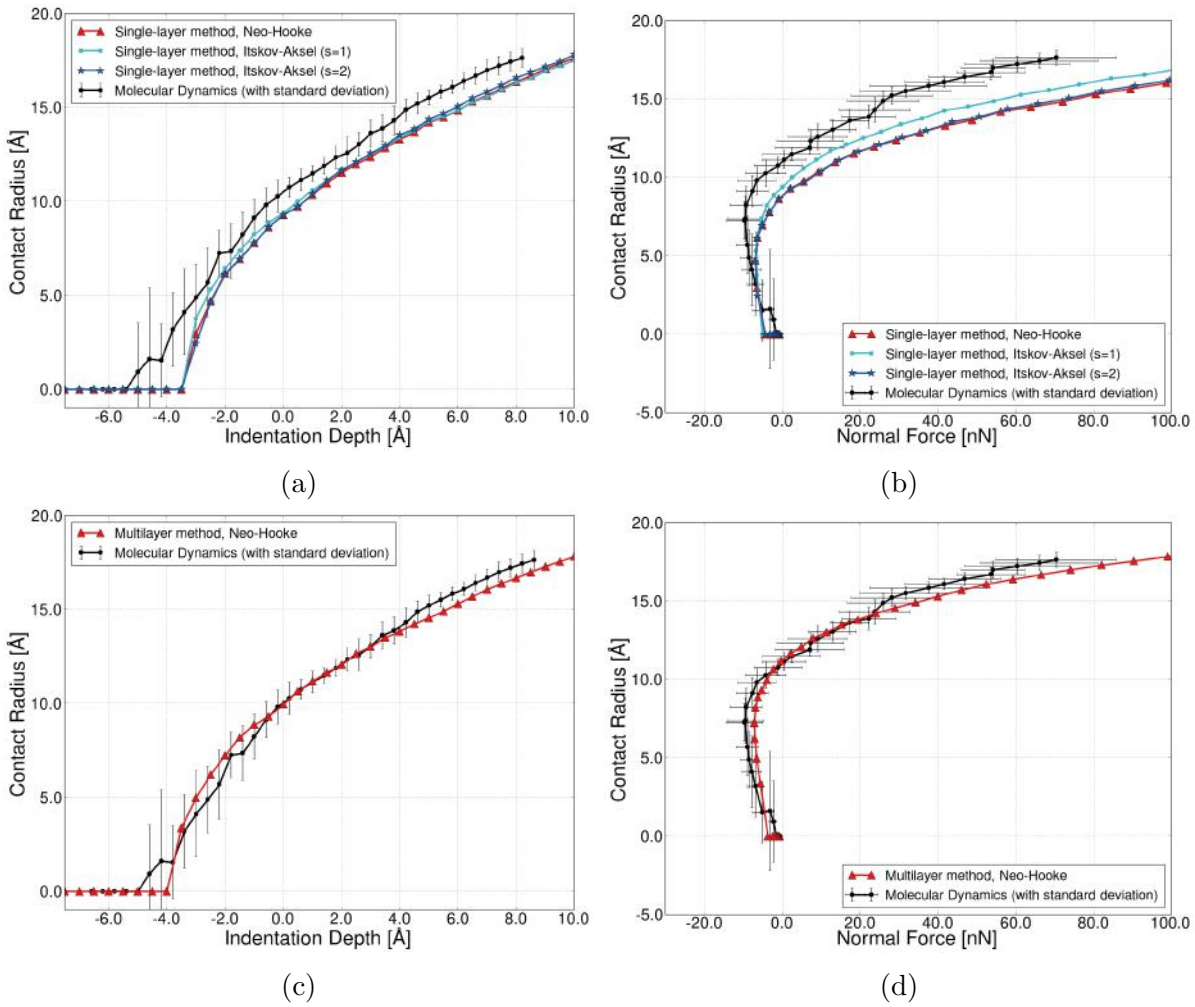

Figure 8: Contact radii for (a,b) various material models obtained from the single-layer method, and for (c,d) a Neo-Hooke model based on the multilayer method. The radius is shown as functions of the indentation depth and the normal force.

5.3. Contact gap

The last benchmark quantity that we want to compare is the contact gap. This is another geometrical measure, describing the separation between the indenter and the polymer surface. At the beginning of the indentation sequence, with the sphere high above the surface, the contact gap is large and steadily decreases as the indenter is pushed down, but always remains positive as the Lennard-Jones forces become infinitely repulsive. We choose the following definition for the atomistic contact gap. Consider a cylindrical column of radius $R/2$, with axis normal to the surface and centered under the indenter. All atoms in the SAM lying within this cylinder are selected; of these, we keep the 10% of atoms closest to the indenter center. This procedure is repeated for 100 snapshots separated by 2000 time steps each. Collecting the positions of these remaining atoms over time yields a set of coordinates $\mathbf{x}_1, \ldots, \mathbf{x}_A$. The gap is then given by

$$\frac{1}{A}\sum_{i=1}^{A}\big(\|\mathbf{c}-\mathbf{x}_i\|-R\big), \tag{27}$$

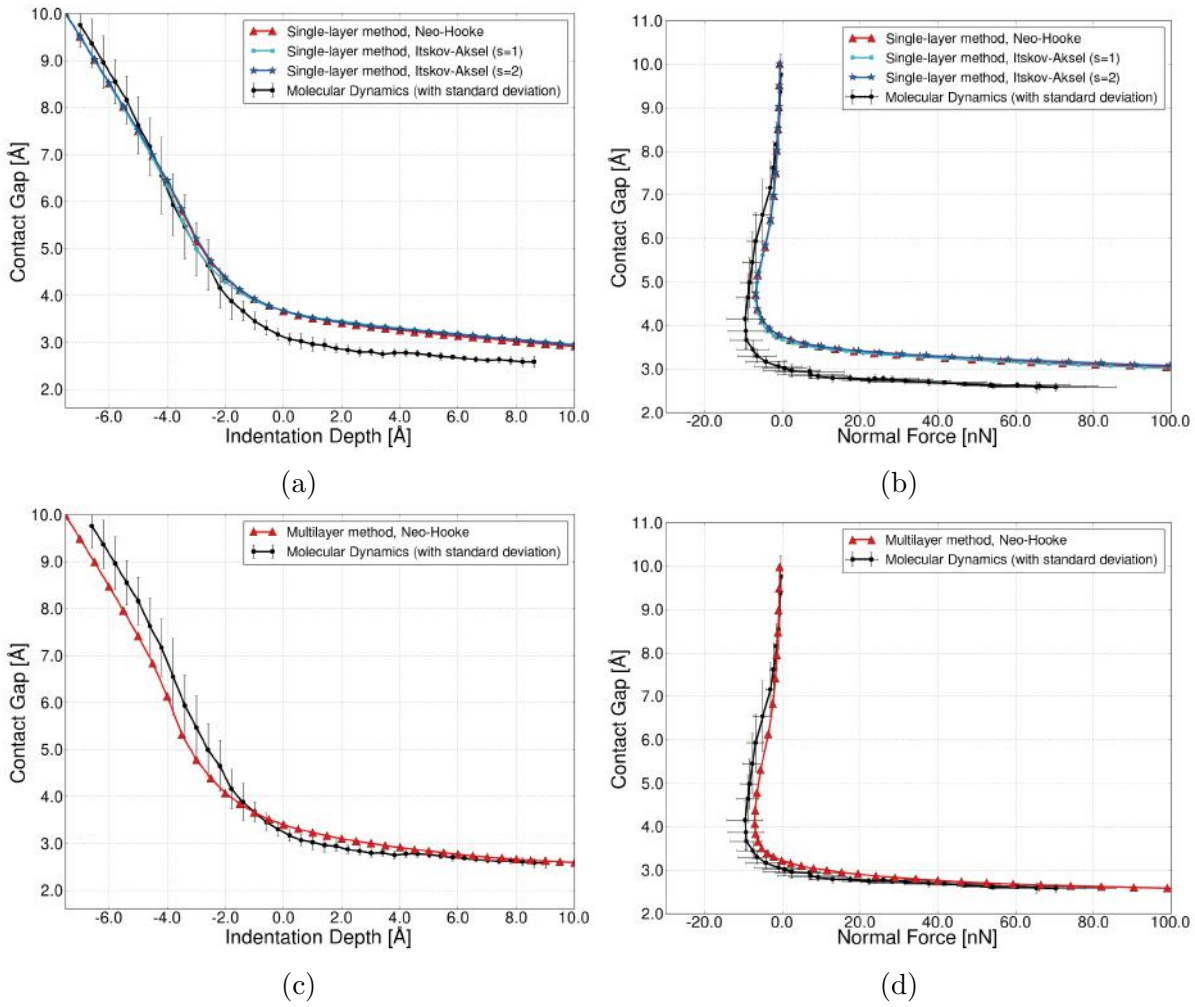

Figure 9: Contact gaps for (a,b) various material models obtained from the single-layer method, and for (c,d) Neo-Hooke parameters based on the multilayer method. All curve plots are created with [81].

where $\mathbf{c}$ and R are the center and radius of the indenter. The gap can be defined similarly for FEM simulations: for the solution configuration $\boldsymbol{\varphi}^*$, we consider a cylinder of radius $R/2$, with axis normal to the cuboid $\mathcal{B}_0^{(1)}$ and passing through the indenter center. All quadrature points lying within this cylinder are selected. From the quadrature points in this intersection, the fraction 10% of points closest to the indenter center is chosen and used to compute the gap again via formula (27).

The resulting curves for the single-layer and multilayer methods are shown in figures 9a,b and 9c,d, respectively. For both the contact radius and contact gap, we see the same trend as for the normal forces: a homogeneous material law obtained by the single-layer method gives moderate qualitative agreement, but the multilayer method more accurately represents the entire indentation process. Also note that a nearly linear relationship between gap and indentation depth ensues in figures 9a,c for large separations of the indenter, whence a finite discrepancy between the curves remains.

5.4. Summary of possible error sources

In both the single-layer and multilayer methods, a set of virtual experiments defines a regime of strains over which the fitted material is expected to show good mean agreement. However, if the material parameters are later used in a specific application, such as nanoindentation, a different strain range may be more important, although such information is rarely known in advance. On the other hand, we can determine *a posteriori* which set of virtual experiments led to the best agreement and spanned the most relevant strain regime. A main assumption in determining hyperelastic material parameters was that the virtual deformation experiments result in a well-equilibrated state. If, however, the simulation time is too short to achieve equilibration, the calculated stresses may not be sufficiently relaxed and a dependency on the applied deformation rate could occur. In ancillary numerical tests we have repeated the deformation experiments of section 4.2 for the multilayer method with twice the simulation time (total of 12 ns instead of 6 ns). While this was not an exhaustive test, no significant differences between the extracted Neo-Hooke bulk and shear moduli were found; this could mean that the apparent influence of the choice of deformations on material parameters has its roots mainly in actual structural changes of the material's response. A possible extension would thus be to have the material parameters $\boldsymbol{\lambda}$ explicitly depend on the deformation, yielding constitutive relations $\mathbf{S} = \bar{\mathbf{S}}(\mathbf{C}; \boldsymbol{\lambda}(\mathbf{C}))$ or $\mathbf{S} = \bar{\mathbf{S}}(\mathbf{C}; \boldsymbol{\lambda}(\mathbf{C}, \mathbf{X}))$, respectively.

The continuum surrogate model introduces several further approximations. For example, interactions between indenter and SAM particles are written as an integral and the particle density within the latter is only estimated. Furthermore, the shape of the SAM is described as a simple cuboid; future endeavors could focus on resolving the geometric details of the monolayer more accurately.

6. Conclusions

We have constructed a continuum mechanical model for nanoindentation in a self-assembled monolayer that calculates contact quantities to good agreement with MD simulations. These contact quantitites have been defined to be transferable between the atomistic and continuum regimes. We have seen that the assumption of homogeneous material behavior in the single-layer method leads already to useful results. However, the situation can be improved by allowing the material model parameters to vary as a function of height within the monolayer. Using the multilayer method, even a simple material model like Neo-Hooke permitted the semi-quantitative reconstruction of normal forces and geometrical quantities. Furthermore, neglecting anisotropy did not have a large influence on the calculated continuum curves. It seems that a reasonable determination of per-layer bulk and shear moduli provide sufficient information for modeling a SAM with long ($n = 150$), entwined chains.

Our methodology was designed to use only interatomic potentials as input data. From this, a constitutive law modeling the mechanical response of a self-assembled monolayer or similar film-like structures can be obtained. Beyond the choice of hyperelastic functional form, both testing methods are flexible in the choice of the sets

of virtual deformation experiments. In this sense, this procedure cannot be classified as strictly predictive, but it is certainly possible to determine guidelines for the relevant range of virtual experiments for comparable systems. The approach might also be useful to adjust material parameters based on atomistic nanoindentation simulations of a smaller system, which are then used to solve a continuum problem involving a much larger surface. However, one must then be aware of possible new size effects in the scaled problem. It is furthermore worthwhile to mention that various algorithmic parameters of the multilayer method, like the number L of sublayers, the number P of points sampled in each of these sublayers or the choice of the norm $\|\cdot\|_*$ used to define an atomistic neighborhood of a coordinate, may be adjusted. However, we did not observe a strong dependence of the resultant curves on these choices. The additional appendix B gives conditions under which it is justified to model polymeric material behavior as hyperelastic.

In summary, we have shown how to obtain suitable hyperelastic constitutive relations for SAMs. Afterward, contact quantities can be calculated more efficiently using the continuum surrogate instead of the original MD simulation. In particular, the atomistic system in our example consists of 176,400 real-valued degrees of freedom, explicitly integrated over 24 million timesteps in an explicit fashion. The continuum system employs 131,733 scalar unknowns, but only a few Newton iterations are needed at each displacement level. As it is hard to compare the efficiency of a mature MD code with a relatively simple self-written finite element code, we note that our nanoindentation simulation with the former took several days on a 64-core machine, whereas the latter ran on four cores in a few hours. In future applications, it would be interesting to also study dynamical contact quantities, most notably friction. This would require determining a friction law from molecular dynamics, which amounts to essentially another parameter fitting task.

7. Acknowledgements

The authors are grateful to the German Research Foundation (DFG) for supporting this research under projects GSC 111 and SA1822/5-1.

A. Material-specific values

Symbol	Meaning	Value
k_q	bond energy	$8071.19\,\mathrm{kcal\,mol^{-1}\,\AA^{-2}}$
q^0	equilibrium bond distance	$1.53\,\mathrm{\AA}$
k_θ	angle energy	$60\,\mathrm{kcal\,mol^{-1}\,rad^{-2}}$
θ^0	equilibrium angle	109.5°
A_1	dihedral energy coefficients	$1.736\,\mathrm{kcal\,mol^{-1}}$
A_2		$-4.490\,\mathrm{kcal\,mol^{-1}}$
A_3		$0.776\,\mathrm{kcal\,mol^{-1}}$
A_4		$6.990\,\mathrm{kcal\,mol^{-1}}$
A_5		0
ε	Lennard-Jones strength	$2.583\,\mathrm{kcal\,mol^{-1}}$
σ	Lennard-Jones separation	$4.01\,\mathrm{\AA}$

Table 2: The used values for the interatomic potential for bonded interactions between polymer beads in terms of (1), as well as the Lennard-Jones parameters for non-bonded interactions.

Constitutive model	Parameter	Value
Neo-Hooke	κ (bulk modulus)	107.82 GPa
	μ (shear modulus)	9.76 GPa
Itskov-Aksel (s=1)	μ_1	19.83 GPa
	$w_1^{(1)}$	0.40096
	$w_2^{(1)} = 1 - w_1^{(1)}$	0.59904
	α_1	6.1798
	β_1	1.0
	γ_1	3.4906
Itskov-Aksel (s=2)	μ_1	6.98 GPa
	$w_1^{(1)}$	1.0
	α_1	3.1127
	β_1	1.0
	γ_1	0.78619
	μ_2	15.48 GPa
	$w_1^{(2)}$	$2.8581 \cdot 10^{-12}$
	α_2	1.0
	β_2	2.535
	γ_2	3.8928

Table 3: Single-layer method: Identified material parameters for various constitutive laws.

Sublayer	Depth of sublayer	κ (bulk modulus)	μ (shear modulus)
1 (closest to substrate)	$X_3 \leq 17.58\,\mathrm{\AA}$	102.64 GPa	11.13 GPa
2	$17.58\,\mathrm{\AA} < X_3 \leq 22.17\,\mathrm{\AA}$	114.73 GPa	8.52 GPa
3	$22.17\,\mathrm{\AA} < X_3 \leq 27.75\,\mathrm{\AA}$	106.96 GPa	9.75 GPa
4	$26.75\,\mathrm{\AA} < X_3 \leq 31.33\,\mathrm{\AA}$	104.72 GPa	7.44 GPa
5	$31.33\,\mathrm{\AA} < X_3 \leq 35.92\,\mathrm{\AA}$	93.38 GPa	5.77 GPa
6 (closest to free surface)	$35.92\,\mathrm{\AA} < X_3$	7.32 GPa	4.89 GPa

Table 4: Multilayer method: Identified Neo-Hooke material parameters for each sublayer.

B. Continuum mechanical remarks

In this section, we informally justify using a hyperelastic material model in the continuum-mechanical formulation of the quasi-static nanoindentation problem (4). Our starting point is the general time-dependent equation of balance of linear momentum, which for a body $\mathcal{B}_0$ can be written in material form as

$$\mathrm{Div}_{\mathbf{X}}\,\mathbf{P}(\mathbf{X},t)+\mathbf{B}(\mathbf{X},t)=\rho_0(\mathbf{X})\mathbf{A}(\mathbf{X},t),\quad \mathbf{X}\in\mathcal{B}_0, t\in I_T=[0,t_{\max}]. \tag{28}$$

Here, $\mathbf{B}(\mathbf{X},t)$ is a body force per reference volume (body force per mass times reference-mass density ρ_0) that may vary over time. We have seen that for nanoindentation, this term could, for example, describe the Lennard-Jones interactions between surface and indenter. On the right hand side, $\mathbf{A}(\mathbf{X},t)=\partial^2\boldsymbol{\varphi}(\mathbf{X},t)/\partial t^2$ denotes the material acceleration. Furthermore, time-independent Dirichlet, Neumann and periodic boundary conditions on parts of the boundary $\partial\mathcal{B}_0$ are admitted. As we are interested in polymers, which frequently exhibit viscoelastic behavior such as creep, the stress response $\mathbf{P}(\mathbf{X},t)$ to a deformation should relax over time when boundary conditions remain constant. Thus, if the external body forces remain unchanged for a long enough time, the stress will eventually converge [82]. If one is solely interested in just this terminal behavior, it is possible to determine an "effective" hyperelastic material model that relates deformations to their converged stress values. This requires that we restrict on the deformations that the system undergoes during the indentation. One approach for modeling viscoelasticity is provided by the thermodynamic framework of Coleman and Gurtin [83], which has been used for other constitutive models [84, 85], and we assume that the SAM can be phenomenologically described by this theory. Coleman and Gurtin [83] assume that the Helmholtz free energy at (quasi-)equilibrium is given as a function of the deformation gradient $\mathbf{F}$, the temperature T, as well as an additional vector of *internal state variables* $\boldsymbol{\alpha}=(\alpha_1,\dots,\alpha_m)$. As the number of particles in a closed thermodynamic system is constant, the free energy can be written as $\Psi=\Psi(\mathbf{F},T,\boldsymbol{\alpha})$. The internal state variables are governed by ordinary differential equations,

$$\dot{\boldsymbol{\alpha}}(t)=f\big(\mathbf{F}(t),T,\boldsymbol{\alpha}(t)\big),\quad \boldsymbol{\alpha}(0)=\boldsymbol{\alpha}_0, \tag{29}$$

and we abbreviate the corresponding solution as $\boldsymbol{\alpha}(t)=\widehat{\boldsymbol{\alpha}}(t,\mathbf{F}(\cdot),T,\boldsymbol{\alpha}_0)$. In this appendix, we review the original reference [83] and state additional assumptions to obtain an effective hyperelastic material model that describes the final stress response after relaxation. As our system is isothermal, we let $T\equiv T_0$.

We study the evolution of the free energy over time accompanying a deformation $t\mapsto\mathbf{F}_{\mathrm{def}}(t)$. Suppose that we have a certain set of "feasible" deformation processes, which might for example describe particularly smooth and slow deformations of our thermodynamic system. To obtain the sought hyperelastic material model, we impose the following assumptions:

(i) There exists a set $\mathcal{F}$ of "relevant" deformation gradients such that all feasible deformation processes satisfy $\mathbf{F}_{\mathrm{def}}(t)\in\mathcal{F}$ for all t.

(ii) There exists a mapping $\boldsymbol{\alpha}_*(\cdot, T_0) : \mathcal{F} \to \mathbb{R}^m$ that associates with each deformation gradient an equilibrium of (29): $f(\mathbf{F}, T_0, \boldsymbol{\alpha}_*(\mathbf{F}, T_0)) = 0$ for all $\mathbf{F} \in \mathcal{F}$. In [83], this mapping is called an *equilibrium response function*. Furthermore, each equilibrium is asymptotically stable: there exists an open neighborhood $\mathcal{N} = \mathcal{N}(\mathbf{F}, T_0)$ around $\boldsymbol{\alpha}_*(\mathbf{F}, T_0)$ such that all nearby internal states $\widetilde{\boldsymbol{\alpha}} \in \mathcal{N}(\mathbf{F}, T_0)$ lead to the terminal value $\lim_{t\to\infty} \widehat{\boldsymbol{\alpha}}(t, \mathbf{F}, T_0, \widetilde{\boldsymbol{\alpha}}) = \boldsymbol{\alpha}_*(\mathbf{F}, T_0)$ when $\mathbf{F}$ is held fixed.

(iii) Each feasible deformation process drives the internal state to its equilibrium response value:

$$\lim_{t\to\infty} \widehat{\boldsymbol{\alpha}}\Big(t, \mathbf{F}_{\mathrm{def}}(\cdot), T_0, \boldsymbol{\alpha}_*\big(\mathbf{F}_{\mathrm{def}}(0), T_0\big)\Big) = \boldsymbol{\alpha}_*(\mathbf{F}_{\mathrm{def}}(\infty), T_0) \tag{30}$$

Condition (iii) says that a feasible deformation process may visit various internal states, but in the infinite-time limit will always terminate at $\boldsymbol{\alpha}_*(\mathbf{F}_{\mathrm{def}}(\infty), T_0)$.

We can readily show that the terminal free energy as well as the terminal first Piola-Kirchhoff stress associated with a feasible deformation process $\mathbf{F}_{\mathrm{def}}$ can be expressed in terms only of its final value $\mathbf{F}_\infty = \mathbf{F}_{\mathrm{def}}(\infty) = \lim_{t\to\infty} \mathbf{F}_{\mathrm{def}}(t)$ and the temperature:

$$\Psi_\infty(\mathbf{F}, T_0) := \Psi(\mathbf{F}, T_0, \boldsymbol{\alpha}_*(\mathbf{F}, T_0)), \quad \mathbf{P}_\infty(\mathbf{F}, T_0) := \frac{1}{V_0}\frac{\partial}{\partial \mathbf{F}}\Psi_\infty(\mathbf{F}, T_0). \tag{31}$$

By V_0 we denote the reference (undeformed) volume associated with the thermodynamic system. Now we consider a feasible deformation process $\mathbf{F}_{\mathrm{def}}$ with initial value $\mathbf{F}_0 = \mathbf{F}_{\mathrm{def}}(0)$ and final value $\mathbf{F}_\infty = \lim_{t\to\infty} \mathbf{F}_{\mathrm{def}}(t)$. If the internal state starts at $\boldsymbol{\alpha}_0 := \boldsymbol{\alpha}_*(\mathbf{F}_0, T_0)$, the free energy of the system along this deformation process is given by

$$\overline{\Psi}(t) := \Psi\Big(\mathbf{F}_{\mathrm{def}}(t), T_0, \widehat{\boldsymbol{\alpha}}\big(t, \mathbf{F}_{\mathrm{def}}(\cdot), T_0, \boldsymbol{\alpha}_0\big)\Big). \tag{32}$$

Consequently, using condition (iii), the final free energy will be

$$\overline{\Psi}(\infty) = \Psi\big(\mathbf{F}_\infty, T_0, \boldsymbol{\alpha}_*(\mathbf{F}_\infty, T_0)\big) = \Psi_\infty(\mathbf{F}_\infty, T_0) \tag{33}$$

and thus depends only on the final deformation gradient and not on the history of the deformation process. In addition, we can also study a constant deformation process with $\mathbf{F} \in \mathcal{F}$. If the internal state is initially at some $\widetilde{\boldsymbol{\alpha}} \in \mathcal{N}(\mathbf{F}, T_0)$ then the free energy over time is

$$\overline{\Psi}(t) := \Psi\big(\mathbf{F}, T_0, \widehat{\boldsymbol{\alpha}}(t, \mathbf{F}, T_0, \widetilde{\boldsymbol{\alpha}})\big). \tag{34}$$

By condition (ii) it transitions from $\overline{\Psi}(0) = \Psi(\mathbf{F}, T_0, \widetilde{\boldsymbol{\alpha}})$ into $\overline{\Psi}(\infty) = \Psi(\mathbf{F}, T_0, \boldsymbol{\alpha}_*(\mathbf{F}, T_0))$. Based on the Clausius-Duhem inequality, Coleman and Gurtin show [83, Eq. 6.8] that, for constant deformation states, the free energy can only decrease over time and is only dissipated internally. Then, since $\Psi(\mathbf{F}, T_0, \boldsymbol{\alpha}_*(\mathbf{F}, T_0)) \leq \Psi(\mathbf{F}, T_0, \widetilde{\boldsymbol{\alpha}})$ for all $\widetilde{\boldsymbol{\alpha}} \in \mathcal{N}(\mathbf{F}, T_0)$, we conclude that the *equation of internal equilibrium* holds:

$$\partial_{\boldsymbol{\alpha}} \Psi\big(\mathbf{F}, T_0, \boldsymbol{\alpha}_*(\mathbf{F}, T_0)\big) = \mathbf{0} \tag{35}$$

For the terminal stress, the previous statement immediately yields the relationship

$$\mathbf{P}\big(\mathbf{F}, T_0, \boldsymbol{\alpha}_*(\mathbf{F}, T_0)\big) = \frac{1}{V_0}\partial_{\mathbf{F}} \Psi\big(\mathbf{F}, T_0, \boldsymbol{\alpha}_*(\mathbf{F}, T_0)\big) = \frac{1}{V_0}\frac{\partial}{\partial \mathbf{F}}\Psi_\infty(\mathbf{F}, T_0) = \mathbf{P}_\infty(\mathbf{F}, T_0), \tag{36}$$

for any $\mathbf{F} \in \mathcal{F}$. Returning to the deformation process $\mathbf{F}_{\mathrm{def}}(\cdot)$, we have

$$\begin{aligned}\lim_{t\to\infty} \mathbf{P}\Big(\mathbf{F}_{\mathrm{def}}(t), T_0, \widehat{\boldsymbol{\alpha}}\big(t, \mathbf{F}_{\mathrm{def}}(\cdot), T_0, \boldsymbol{\alpha}_0\big)\Big) &= \mathbf{P}\Big(\mathbf{F}_\infty, T_0, \lim_{t\to\infty} \widehat{\boldsymbol{\alpha}}\big(t, \mathbf{F}_{\mathrm{def}}(\cdot), T_0, \boldsymbol{\alpha}_0\big)\Big) \\ &= \mathbf{P}\big(\mathbf{F}_\infty, T_0, \boldsymbol{\alpha}_*(\mathbf{F}_\infty, T_0)\big) \\ &= \mathbf{P}_\infty(\mathbf{F}_\infty, T_0);\end{aligned}$$

that is, the terminal stress is indeed given through the mapping $\mathbf{P}_\infty$. Since it is obtained as the derivative of the final strain energy density Ψ_∞/V_0 the functional relationship is hyperelastic. The preceding reasoning was carried out for an individual thermodynamic system, whereas the continuum assumes that there is a local thermodynamic system associated with each continuum point $\mathbf{X}$. Therefore, since the temperature is constant, the effective stress may be written in location-dependent form as $\mathbf{P}_\infty = \mathbf{P}_\infty(\mathbf{F}, \mathbf{X})$.

We now consider the limit $t \to \infty$ of the dynamic balance equation (28), which is valid if the observation time is very large compared to the equilibration time:

$$\mathrm{Div}_{\mathbf{X}}\, \mathbf{P}(\mathbf{X}) + \mathbf{B}(\mathbf{X}) = \mathbf{0}, \quad \mathbf{X} \in \mathcal{B}_0. \tag{37}$$

In particular, for our nanoindentation problem, this corresponds to the form (6), where the equilibrium stress relation is here written as $\mathbf{P}(\mathbf{X}) = \mathbf{P}_\infty(\mathbf{F}, \mathbf{X})$, which determines the terminal stress value as a function of the local deformation $\mathbf{F} = \nabla\boldsymbol{\varphi}(\mathbf{X})$.

For the nanoindentation problem not only can we consider a single position of the indenter, reflected by particular body forces $\mathbf{B}$, but a whole sequence of successive indentation steps with different indenter positions. More specifically, we are interested in a discrete set of indentation depths $\tau \in \{\tau_1, \ldots, \tau_K\}$:

$$\mathrm{Div}_{\mathbf{X}}\, \mathbf{P}_\infty\big(\nabla\boldsymbol{\varphi}(\mathbf{X}), \mathbf{X}\big) + \mathbf{B}(\mathbf{X}; \tau) = \mathbf{0}, \quad \mathbf{X} \in \mathcal{B}_0. \tag{38}$$

Hence, increasing the depth level τ and solving a sequence of stationary problems corresponds to a quasi-static process where the indenter is pushed down very slowly compared to the equilibration time scale. Therefore, the stresses determined in this process should always be close to the relaxed, final values for each indenter position. These terminal stress values are $\mathbf{P}_\infty$ in (38), and we have thus described possible circumstances under which a hyperelastic constitutive relation can replace the general time-dependent one in the infinite-time limit.

References

[1] Izabela Szlufarska, Michael Chandross, and Robert W Carpick. Recent advances in single-asperity nanotribology. *Journal of Physics D: Applied Physics*, 41(12):123001, 2008. URL http://stacks.iop.org/0022-3727/41/i=12/a=123001.

[2] Kenneth Holmberg, Peter Andersson, and Ali Erdemir. Global energy consumption due to friction in passenger cars. *Tribology International*, 47:221–234, 2012.

[3] B Bhushan. Nanotribology and nanomechanics: An introduction, 2005.

[4] Howard Brenner. The slow motion of a sphere through a viscous fluid towards a plane surface. *Chemical Engineering Science*, 16(3):242–251, 1961.

[5] J. Matthew D. Lane, Ahmed E. Ismail, Michael Chandross, Christian D. Lorenz, and Gary S. Grest. Forces between functionalized silica nanoparticles in solution. *Phys. Rev. E*, 79:050501, May 2009. doi: 10.1103/PhysRevE.79.050501. URL http://link.aps.org/doi/10.1103/PhysRevE.79.050501.

[6] J Christopher Love, Lara A Estroff, Jennah K Kriebel, Ralph G Nuzzo, and George M Whitesides. Self-Assembled Monolayers of Thiolates on Metals as a Form of Nanotechnology. *Chemical Reviews*, 105(4):1103–1170, April 2005.

[7] Ahmed E. Ismail, Gary S. Grest, and Mark J. Stevens. Structure and dynamics of water near the interface with oligo(ethylene oxide) self-assembled monolayers. *Langmuir*, 23(16):8508–8514, 2007. doi: 10.1021/la700829r. URL http://pubs.acs.org/doi/abs/10.1021/la700829r.

[8] Brandon L Peters, J Matthew D Lane, Ahmed E Ismail, and Gary S Grest. Fully atomistic simulations of the response of silica nanoparticle coatings to alkane solvents. *Langmuir*, 28(50):17443–17449, 2012.

[9] Mingji Wang, Kenneth M Liechti, John M White, and Robb M Winter. Nanoindentation of polymeric thin films with an interfacial force microscope. *Journal of the Mechanics and Physics of Solids*, 52(10):2329–2354, 2004.

[10] Julia Deuschle, Susan Enders, and Eduard Arzt. Surface detection in nanoindentation of soft polymers. *Journal of Materials Research*, 22(11):3107–3119, 2007. doi: 10.1557/JMR.2007.0394. URL http://dx.doi.org/10.1557/JMR.2007.0394.

[11] Frank W DelRio, Cherno Jaye, Daniel A Fischer, and Robert F Cook. Elastic and adhesive properties of alkanethiol self-assembled monolayers on gold. *Applied Physics Letters*, 94(13):131909–131909, 2009.

[12] Frank W DelRio, David M Rampulla, Cherno Jaye, Gheorghe Stan, Richard S Gates, Daniel A Fischer, and Robert F Cook. Structure–property relationships for methyl-terminated alkyl self-assembled monolayers. *Chemical Physics Letters*, 512(4):243–246, 2011.

[13] Michael Chandross, Christian D. Lorenz, Mark J. Stevens, and Gary S. Grest. Simulations of nanotribology with realistic probe tip models. *Langmuir*, 24(4):1240–1246, 2008. doi: 10.1021/la702323y. URL http://pubs.acs.org/doi/abs/10.1021/la702323y. PMID: 18184018.

[14] Anthony C Fischer-Cripps. *Nanoindentation*, volume 1. Springer, 2011.

[15] Jack E. Houston and Hyun I. Kim. Adhesion, friction, and mechanical properties of functionalized alkanethiol self-assembled monolayers. *Accounts of Chemical Research*, 35(7):547–553, 2002. doi: 10.1021/ar9801144. URL http://pubs.acs.org/doi/abs/10.1021/ar9801144.

[16] Ju Li, Alfonso HW Ngan, and Peter Gumbsch. Atomistic modeling of mechanical behavior. *Acta Materialia*, 51(19):5711–5742, 2003.

[17] Michael Chandross, Christian D Lorenz, Mark J Stevens, and Gary S Grest. Probe-

tip induced damage in compliant substrates. *Journal of Manufacturing Science and Engineering*, 132(3), 2010.

[18] Till Junge and Jean-François Molinari. Molecular dynamics nano-scratching of aluminium: a novel quantitative energy-based analysis method. *Procedia IUTAM*, 3:192–204, 2012.

[19] Kenneth Langstreth Johnson. *Contact mechanics*. Cambridge University Press, 1987.

[20] Anthony C Fischer-Cripps. *Introduction to Contact Mechanics*. Springer, 2000.

[21] Noboru Kikuchi and John Tinsley Oden. *Contact Problems in Elasticity*. SIAM, 1988.

[22] Tod A Laursen. *Computational Contact and Impact Mechanics*. Springer, 2002.

[23] Peter Wriggers. *Computational Contact Mechanics*. John Wiley & Sons, 2002.

[24] Roger A. Sauer and Shaofan Li. An atomistically enriched continuum model for nanoscale contact mechanics and its application to contact scaling. *Journal of Nanoscience and Nanotechnology*, 8(7):3757–3773, 2008. doi: doi:10.1166/jnn.2008.014. URL http://www.ingentaconnect.com/content/asp/jnn/2008/00000008/00000007/art00061.

[25] Roger A. Sauer and Peter Wriggers. Formulation and analysis of a three-dimensional finite element implementation for adhesive contact at the nanoscale. *Computer Methods in Applied Mechanics and Engineering*, 198(49–52):3871 – 3883, 2009. ISSN 0045-7825. doi: 10.1016/j.cma.2009.08.019. URL http://www.sciencedirect.com/science/article/pii/S0045782509002631.

[26] Ryan S Elliott, Nicolas Triantafyllidis, and John A Shaw. Stability of crystalline solids — I: Continuum and atomic lattice considerations. *Journal of the Mechanics and Physics of Solids*, 54(1):161–192, 2006.

[27] Guillaume Anciaux and Jean-Francois Molinari. Contact mechanics at the nanoscale, a 3D multiscale approach. *International Journal for Numerical Methods in Engineering*, 79(9):1041–1067, 2009.

[28] SP Xiao and Ted Belytschko. A bridging domain method for coupling continua with molecular dynamics. *Computer Methods in Applied Mechanics and Engineering*, 193 (17):1645–1669, 2004.

[29] G Anciaux, SB Ramisetti, and JF Molinari. A finite temperature bridging domain method for MD-FE coupling and application to a contact problem. *Computer Methods in Applied Mechanics and Engineering*, 205:204–212, 2012.

[30] Wenzhe Shan and Udo Nackenhorst. An adaptive FE–MD model coupling approach. *Computational Mechanics*, 46(4):577–596, 2010.

[31] Ellad B Tadmor, Michael Ortiz, and Rob Phillips. Quasicontinuum analysis of defects in solids. *Philosophical Magazine A*, 73(6):1529–1563, 1996.

[32] Chung-Ting Wang, Sheng-Rui Jian, Jason Shian-Ching Jang, Yi-Shao Lai, and Ping-Feng Yang. Multiscale simulation of nanoindentation on Ni (100) thin film. *Applied Surface Science*, 255(5):3240–3250, 2008.

[33] Binquan Luan and Mark O Robbins. Hybrid atomistic/continuum study of contact and friction between rough solids. *Tribology Letters*, 36(1):1–16, 2009.

[34] GS Smith, EB Tadmor, N Bernstein, and E Kaxiras. Multiscale simulations of silicon nanoindentation. *Acta materialia*, 49(19):4089–4101, 2001.

[35] H Eid, GG Adams, NE McGruer, A Fortini, S Buldyrev, and D Srolovitz. A combined molecular dynamics and finite element analysis of contact and adhesion of a rough sphere and a flat surface. *Tribology Transactions*, 54(6):920–928, 2011.

[36] V B C Tan, X S Zeng, M Deng, K M Lim, and T E Tay. Multiscale modeling of polymers: The Pseudo Amorphous Cell. *Computer Methods in Applied Mechanics and Engineering*, 197(6):536–554, 2008.

[37] P. K. Valavala, T. C. Clancy, G. M. Odegard, and T. S. Gates. Nonlinear multiscale modeling of polymer materials. *International Journal of Solids and Structures*, 44 (3–4):1161 – 1179, 2007. ISSN 0020-7683. doi: 10.1016/j.ijsolstr.2006.06.011. URL http://www.sciencedirect.com/science/article/pii/S0020768306002198.

[38] Mykola Tkachuk and Christian Linder. The maximal advance path constraint for the homogenization of materials with random network microstructure. *Philosophical Magazine*, 92(22):2779–2808, 2012.

[39] Huajian Gao and Patrick Klein. Numerical simulation of crack growth in an isotropic solid with randomized internal cohesive bonds. *Journal of the Mechanics and Physics of Solids*, 46(2):187 – 218, 1998. ISSN 0022-5096. doi: 10.1016/S0022-5096(97)00047-1. URL http://www.sciencedirect.com/science/article/pii/S0022509697000471.

[40] Ellad B. Tadmor and Ronald E. Miller. *Modeling Materials: Continuum, Atomistic and Multiscale Techniques*. Cambridge University Press, 2011.

[41] Zhaoyu Chen and Stefan Diebels. Nanoindentation of hyperelastic polymer layers at finite deformation and parameter re-identification. *Archive of Applied Mechanics*, pages 1–16, 2012. ISSN 0939-1533. URL http://dx.doi.org/10.1007/s00419-012-0613-9. 10.1007/s00419-012-0613-9.

[42] Mingji Wang, Kenneth M. Liechti, Vibha Srinivasan, John M. White, Peter J. Rossky, and Matthew T. Stone. A hybrid continuum-molecular analysis of interfacial force microscope experiments on a self-assembled monolayer. *Journal of Applied Mechanics*, 73(5):769–777, 2006. doi: 10.1115/1.1943435. URL http://link.aip.org/link/?AMJ/73/769/1.

[43] Stephen L Mayo, Barry D Olafson, and William A Goddard. Dreiding: a generic force field for molecular simulations. *Journal of Physical Chemistry*, 94(26):8897–8909, 1990.

[44] William Humphrey, Andrew Dalke, and Klaus Schulten. VMD: Visual Molecular Dynamics. *Journal of Molecular Graphics*, 14:33–38, 1996.

[45] John Stone. An efficient library for parallel ray tracing and animation. Master's thesis, Computer Science Department, University of Missouri-Rolla, April 1998.

[46] Amy Henderson Squillacote. *The ParaView guide: a parallel visualization application*. Kitware, 2007.

[47] H. Hertz. On the contact of elastic solids. *J. Reine Angew. Math.*, 92(156-171):110, 1881.

[48] KL Johnson, K. Kendall, and AD Roberts. Surface energy and the contact of elastic solids. *Proceedings of the Royal Society of London. A. Mathematical and Physical Sciences*, 324(1558):301–313, 1971.

[49] BV Derjaguin, VM Muller, and Y. P. Toporov. Effect of contact deformations on the adhesion of particles. *Journal of Colloid and Interface Science*, 53(2):314–326, 1975.

[50] D. Maugis. Adhesion of spheres: the JKR-DMT transition using a Dugdale model. *Journal of Colloid and Interface Science*, 150(1):243–269, 1992.

[51] Bo NJ Persson. Theory of rubber friction and contact mechanics. *The Journal of Chemical Physics*, 115:3840, 2001.

[52] ED Reedy. Thin-coating contact mechanics with adhesion. *Journal of Materials Research*, 21(10):2660–2668, 2006.

[53] Binquan Luan and Mark O. Robbins. Contact of single asperities with varying adhesion: Comparing continuum mechanics to atomistic simulations. *Phys. Rev. E*, 74:026111, Aug 2006. doi: 10.1103/PhysRevE.74.026111. URL http://link.aps.org/doi/10.1103/PhysRevE.74.026111.

[54] Guangtu Gao, Rachel J Cannara, Robert W Carpick, and Judith A Harrison. Atomic-scale friction on diamond: A comparison of different sliding directions on (001) and (111) surfaces using MD and AFM. *Langmuir*, 23(10):5394–5405, 2007.

[55] C Yang, BNJ Persson, J Israelachvili, and K Rosenberg. Contact mechanics with adhesion: Interfacial separation and contact area. *EPL (Europhysics Letters)*, 84(4): 46004, 2008.

[56] SJV Frankland, VM Harik, GM Odegard, DW Brenner, and TS Gates. The stress–strain behavior of polymer–nanotube composites from molecular dynamics simulation. *Composites Science and Technology*, 63(11):1655–1661, 2003.

[57] D Trias, J Costa, A Turon, and JE Hurtado. Determination of the critical size of a statistical representative volume element (SRVE) for carbon reinforced polymers. *Acta Materialia*, 54(13):3471–3484, 2006.

[58] M Jiang, I Jasiuk, and M Ostoja-Starzewski. Apparent elastic and elastoplastic behavior of periodic composites. *International Journal of Solids and Structures*, 39 (1):199–212, 2002.

[59] Ilker Temizer and Peter Wriggers. A multiscale contact homogenization technique for the modeling of third bodies in the contact interface. *Computer Methods in Applied Mechanics and Engineering*, 198(3):377–396, 2008.

[60] Terrell L. Hill. *Statistical Mechanics: Principles and Selected Applications*. Dover Publications, 1987.

[61] Mark E. Tuckerman. *Statistical Mechanics: Theory and Molecular Simulation*. Oxford University Press, 2010.

[62] J. David Schall and Donald W. Brenner. Atomistic simulation of the influence of pre-existing stress on the interpretation of nanoindentation data. *Journal of Materials Research*, 19(11):3172–3180, 2004. doi: 10.1557/JMR.2004.0410. URL http://dx.doi.org/10.1557/JMR.2004.0410.

[63] P. T. Bauman, J. T. Oden, and S. Prudhomme. Adaptive multiscale modeling of polymeric materials: Arlequin coupling and goals algorithms. *Comput. Methods Appl. Mech. Engrg.*, 198:799–818, 2009.

[64] John R Ray and Aneesur Rahman. Statistical ensembles and molecular dynamics studies of anisotropic solids. *The Journal of chemical physics*, 80:4423, 1984.

[65] Steve Plimpton. Fast parallel algorithms for short-range molecular dynamics. *Journal of Computational Physics*, 117(1):1 – 19, 1995. ISSN 0021-9991. doi: 10.1006/jcph.1995.1039. URL http://lammps.sandia.gov.

[66] R. W. Ogden. *Non-linear elastic deformations*. Dover Publications, 1984.

[67] Mikhail Itskov and Nuri Aksel. A class of orthotropic and transversely isotropic hyperelastic constitutive models based on a polyconvex strain energy function. *International Journal of Solids and Structures*, 41(14):3833–3848, 2004.

[68] RW Ogden, G Saccomandi, and I Sgura. Fitting hyperelastic models to experimental data. *Computational Mechanics*, 34(6):484–502, 2004.

[69] MATLAB. *version 7.11.0 (R2011a)*. The MathWorks Inc., Natick, Massachusetts, 2011.

[70] M. F. Horstemeyer and M. I. Baskes. Strain tensors at the atomic scale. *MRS Proceedings*, 578, 1 1999. ISSN null. doi: 10.1557/PROC-578-15. URL http://journals.cambridge.org/article_S1946427400297832.

[71] PM Gullett, MF Horstemeyer, MI Baskes, and H Fang. A deformation gradient tensor and strain tensors for atomistic simulations. *Modelling and Simulation in Materials Science and Engineering*, 16(1):015001, 2008.

[72] Jonathan A. Zimmerman, Douglas J. Bammann, and Huajian Gao. Deformation gradients for continuum mechanical analysis of atomistic simulations. *International Journal of Solids and Structures*, 46(2):238 – 253, 2009. ISSN 0020-7683. doi: 10.1016/j.ijsolstr.2008.08.036. URL http://www.sciencedirect.com/science/article/pii/S002076830800348X.

[73] JA Zimmerman, EB Webb III, JJ Hoyt, RE Jones, PA Klein, and DJ Bammann. Calculation of stress in atomistic simulation. *Modelling and Simulation in Materials Science and Engineering*, 12(4):319–332, 2004.

[74] Jonathan A Zimmerman, Reese E Jones, and Jeremy A Templeton. A material frame approach for evaluating continuum variables in atomistic simulations. *Journal of Computational Physics*, 229(6):2364–2389, 2010.

[75] Nikhil Chandra Admal and Ellad B Tadmor. A unified interpretation of stress in molecular systems. *Journal of Elasticity*, 100(1-2):63–143, 2010.

[76] D Hossain, MA Tschopp, DK Ward, JL Bouvard, P Wang, and MF Horstemeyer. Molecular dynamics simulations of deformation mechanisms of amorphous polyethylene. *Polymer*, 51(25):6071–6083, 2010.

[77] B. S. Kirk, J. W. Peterson, R. H. Stogner, and G. F. Carey. `libMesh`: A C++ Library for Parallel Adaptive Mesh Refinement/Coarsening Simulations. *Engineering with Computers*, 22(3–4):237–254, 2006.

[78] Satish Balay, William D. Gropp, Lois Curfman McInnes, and Barry F. Smith. Efficient management of parallelism in object oriented numerical software libraries. In E. Arge, A. M. Bruaset, and H. P. Langtangen, editors, *Modern Software Tools in Scientific Computing*, pages 163–202. Birkhäuser Press, 1997.

[79] Satish Balay, Jed Brown, Kris Buschelman, Victor Eijkhout, William D. Gropp, Dinesh Kaushik, Matthew G. Knepley, Lois Curfman McInnes, Barry F. Smith, and Hong Zhang. PETSc users manual. Technical Report ANL-95/11 - Revision 3.4, Argonne National Laboratory, 2013.

[80] SM Foiles, MI Baskes, and MS Daw. Embedded-atom-method functions for the fcc metals Cu, Ag, Au, Ni, Pd, Pt, and their alloys. *Physical Review B*, 33(12):7983, 1986.

[81] J. D. Hunter. Matplotlib: A 2d graphics environment. *Computing In Science & Engineering*, 9(3):90–95, 2007.

[82] Gert R Strobl. *The Physics of Polymers: Concepts for Understanding Their Structures and Behavior*. Springer Berlin, 2007.

[83] B D Coleman and M E Gurtin. Thermodynamics with internal state variables. *Journal of Chemical Physics*, 47:597–613, 1967.

[84] J. C. Simo. On a fully three-dimensional finite-strain viscoelastic damage model: Formulation and computational aspects. *Computer Methods in Applied Mechanics and Engineering*, 60(2):153–173, 1987.

[85] Stefanie Reese and Sanjay Govindjee. Theoretical and numerical aspects in the thermo-viscoelastic material behaviour of rubber-like polymers. *Mechanics of Time-Dependent Materials*, 1(4):357–396, 1997.